Curing-dependent thermo-viscoelastic and shrinkage behaviour of photopolymers

Kubra Sekmen, Thomas Rehbein, Michael Johlitz, Alexander Lion, Andrei Constantinescu

Curing-dependent thermo-viscoelastic and shrinkage behaviour of photopolymers

Kubra Sekmen[a], Thomas Rehbein[b], Michael Johlitz[b], Alexander Lion[b], Andrei Constantinescu[a,*]

[a]*Laboratoire de Mécanique des Solides, CNRS, École Polytechnique, Institut Polytechnique de Paris, Route de Saclay, Palaiseau, 91128, France*
[b]*Department of Aerospace Engineering, Institute of Mechanics, Bundeswehr University Munich, Werner-Heisenberg-Weg 39, Neubiberg, 85577, Germany*

Abstract

This study investigates the influence of curing on the thermo-viscoelastic properties and chemical shrinkage of a commercially available photopolymer resin used in SLA and DLP 3D printing and presents a modelling approach for predicting material properties. UV rheometer and DMA measurements were performed to investigate the viscoelastic properties of the photopolymer material as a function of temperature, degree of cure, and frequency. Time-temperature and time-cure superposition principles were applied to the experimental results. In addition, the chemical shrinkage behaviour was studied by the UV rheometer as a function of the degree of cure and temperature, and a model equation was proposed based on these parameters. Our experimental findings have led to the development of constitutive equations for the complete material behaviour.

Keywords: Photopolymer, Curing, Viscoelastic constitutive law, Shrinkage strain

*Corresponding author.
Email addresses: kubra.sekmen@polytechnique.edu (Kubra Sekmen), rehbein@unibw.de (Thomas Rehbein), michael.johlitz@unibw.de (Michael Johlitz), alexander.lion@unibw.de (Alexander Lion), andrei.constantinescu@polytechnique.edu (Andrei Constantinescu)

1. Introduction

A tremendous advancement in additive manufacturing (AM) technologies over the past few decades has reshaped the way industrial products are created, enabling the production of parts with remarkable accuracy that is not achievable with conventional manufacturing techniques [1, 2]. The primary characteristic of additive manufacturing is the layer-by-layer fabrication of three-dimensional structures as opposed to the traditional production based on subtractive or formative material processing. This cutting-edge manufacturing method enables innovative designs that cannot be obtained with traditional manufacturing techniques, such as 3D printing of lightweight lattice structures known for their superior mechanical properties for a given density or weight [3].

Particularly, curing of a liquid monomer resin into a solid polymer through photopolymerization allows manufacturing of parts with a resolution of layer thickness varying from 10 to 200 µm that can be achieved today for affordable prices [4]. According to the methods of layer deposition, pattern formation principles, and operating systems, photocuring-based 3D printing uses a variety of techniques, such as stereolithography apparatus (SLA) [5], digital light processing (DLP) [6], polyjet printing (PJP) [7], two-photon lithography (TPL) [8], UV-assisted direct ink writing (DIW) [9], continuous liquid interface production (CLIP) [10] and liquid crystal display (LCD) [11]. Fast curing at room temperature, low energy consumption and spatial and temporal control over photopolymerization are all highly desirable in a wide range of industrial applications, including dental materials [12], consumer goods such as shoes and custom insoles [13], coatings [14], biomedical devices and tissue scaffolds [15], metamaterials [16], piezoelectric materials [17] and lithium-ion batteries for aerospace applications [18].

The growing demand for photopolymerization-based 3D printing necessitates special consideration in advanced applications requiring precise control of final material properties, as well as understanding and modelling of the mechanical properties related to the UV curing reaction. During the curing reaction, a viscoelastic liquid converts into a viscoelastic solid, resulting in changes in thermomechanical and caloric material behaviour [19]. The polymer chains become packed and crosslinked as a result of this phase change and the newly formed chemical bonds bring the chains closer together, resulting in a reduction in the specific volume known as volume or curing shrinkage. This chemical shrinkage, coupled with other phenomena such as resin compositon,

nonuniform light intensity with depth due to the Beer-Lambert absorption [20] and heterogeneous curing due to nonlinear light intensity, leads to gradients in the mechanical and chemical material properties and ultimately to residual stresses that affect the shape of the final structure in desirable or undesirable ways [21]. The repeatability and reliability of these products are restricted by the fabrication errors in the parts due to the layer-by-layer printing as previously mentioned [22, 23].

Within the scope of the polymerization process, the effects of process parameters, resin composition, and filler particles on the thermal and rheological properties were studied by experimental methods [19, 24, 25, 26, 27, 28]. However, it is both costly and time consuming to perform these tests and find the appropriate experimental approach to predict the final properties of the printed part using different process parameters. To avoid this classical and expensive experimental procedure, simulation tools provide an excellent alternative for the optimization of the process parameters to fabricate desired parts. Nevertheless, due to a lack of understanding, insufficient constitutive models and simulation tools, such problems are often confronted by costly trial-and-error methods. Since the processed materials are viscoelastic for such applications, constitutive models that take into account the time and temperature history, in addition to the printing parameters, are required for the numerical simulations to predict the material behaviour during and after the printing process.

This work aims to overcome these difficulties by proposing a comprehensive viscoelastic model with chemical shrinkage incorporating the highlighted phenomena in temperature-dependent photopolymer curing. The PR48 photopolymer resin under scrutiny in this work has been extensively studied in previous research to investigate anisotropy in the mechanical properties in printed parts [29, 30], resolution of the printed objects [29, 31], bonding of the layers formed during printing [32], as well as to conduct photorheology measurements and determine the cure depth [31, 33, 34]. However, to the best of the authors' knowledge, systematic characterization and modelling of this resin have not been reported in the literature. The model proposed in this work is identified on thermal, viscoelastic and shrinkage experiments for a large parameter range. As a consequence, it is able to predict the influence of process parameters on the final mechanical properties.

This paper is organized as follows: Section 2 presents the commercial photopolymer resin used for the material characterization, a reminder of the curing model performed in the previous study, and the governing equations

of the linear viscoelasticity characterization. Section 3 focuses on the measurements of the viscoelastic properties during the UV curing process and viscoelastic material modelling based on time-cure superposition around the gelation point. Section 4 is devoted to viscoelastic material modelling of different levels of crosslinked solid samples using DMA measurements. Herein, the time-temperature and time-cure superposition principles were applied to macroscopically capture the change in viscoelastic properties during the complete crosslinking reaction. Section 5 provides measurements and modelling of the evolution of the chemical shrinkage of a photopolymer layer as a function of the degree of cure and the temperature, and Section 6 concludes with some closing remarks and future prospects.

2. Methods and theoretical foundations

2.1. Material

The photopolymer resin used in this work is the standard clear thermoset resin PR48 supplied from Colorado Photopolymer Solutions (Boulder, CO, US). PR48 is designed to work with 385-405 nm light in digital light processing (DLP) and stereolithography apparatus (SLA) 3D printers [35]. The chemical structures of the ingredients of the PR48 resin is given in Figure 1 [36].

2.2. Modelling of the crosslinking reaction

The degree of cure $q(t)$ is a scalar measure of the advancement of the crosslinking process driven by chemical reactions and physical processes. It is defined in terms of specific heat flow as:

$$q(t) = \frac{\int_0^t \dot{h}(\tilde{t})\mathrm{d}\tilde{t}}{h_{tot}} \tag{1}$$

where $\dot{h}(\tilde{t})$ is the specific heat flow converted during the curing time t and h_{tot} is the total heat of reaction of fully crosslinked material. We have previously investigated the crosslinking reaction in the photopolymerization process using this relationship and modelled the reaction kinetics [37, 38, 23, 39]. Photo-differential scanning calorimeter (photo-DSC) measurements were conducted to characterize the curing kinetics of the photopolymer resin under several isothermal conditions and constant UV light intensities. The model is briefly described in the following.

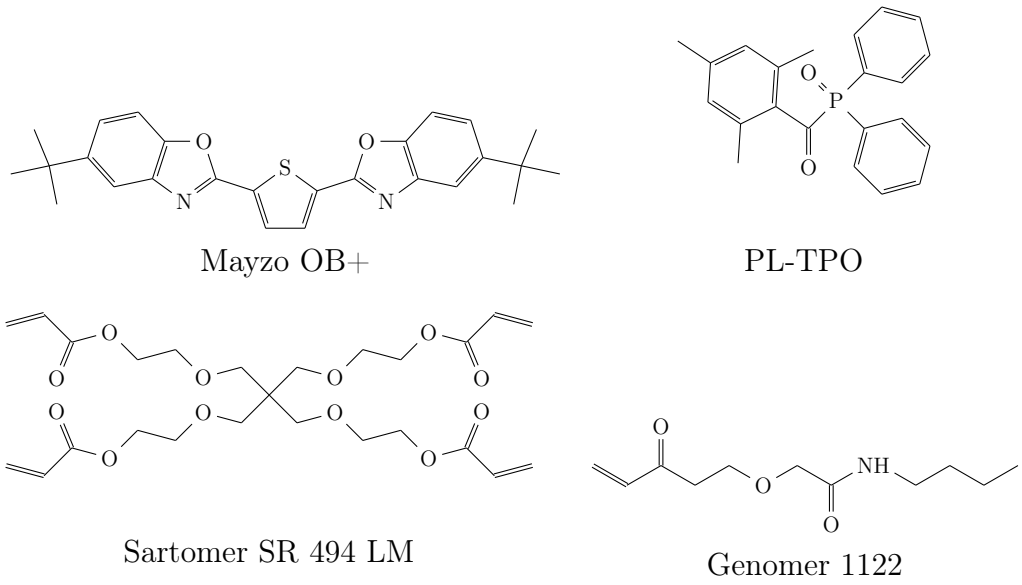

Figure 1: Chemical structures of the ingredients of the PR48 photopolymer material.

A phenomenological equation of $(m+n)^{th}$ order based on the autocatalytic kinetic model was used in order to model the evolution of the degree of cure.

$$\dot{q} = (k_1 + k_2 q^m) \left(q_{\max}(\mathcal{I}, \theta) - q\right)^n \tag{2}$$

In this ordinary differential equation (ODE), $q_{\max}$ indicates the maximum attainable degree of cure as a function of temperature θ in °C and UV light intensity $\mathcal{I}$ in mW/cm^2, k_1 and k_2 are Arrhenius type coefficients that depend on the absolute temperature T in Kelvin and the light intensity as given in Equation 3:

$$k_i(\mathcal{I}, T) = A_i \exp\left(-\frac{E_i}{RT}\right)\left(\frac{\mathcal{I}}{\mathcal{I}_{ref}}\right)^b \quad i = 1, 2 \tag{3}$$

where E_i denotes the activation energies, $R = 8.314$ J/(mol.K) is the universal gas constant, $\mathcal{I}_{ref} = 1$ mW/cm^2 is a reference value to assure the unit consistency of pre-exponential factors A_i, and b is used to fit the experimental data more precisely. Readers are referred to the preceding article [37] for further details on the working principle of the DSC, the experimental procedure, and the parameter identification. Details of the identified parameters can be found Appendix A.

The parameters given in Tables A.8 and A.9 were used to calculate the evolution of the degree of cure during the UV rheometer test using Equations 1, 2 and 3 to analyse the viscoelastic material properties and chemical shrinkage as a function of the degree of cure and temperature. Furthermore, the degrees of cure of the solid samples tested in DMA in Section 4 were calculated using the residual specific heat of reaction h_r measured by classical DSC measurements and the total specific heat of reaction h_{tot} obtained by photo-DSC as follows:

$$q = 1 - \frac{h_r}{h_{tot}} \tag{4}$$

2.3. Linear viscoelasticity characterization

The viscoelastic behaviour of the materials is studied through dynamic tests in which the stress (or strain) resulting from a sinusoidal strain (or stress) is measured in torsional mode. When a viscoelastic material is continuously subjected to a sufficient small sinusoidal shear strain $\gamma(t)$, a steady state will eventually be attained in which the resulting shear stress in the sample $\tau(t)$ is also sinusoidal, with the same angular frequency ω but out of phase with the imposed strain by a shift angle δ. The current temperature and degree of cure of the polymer, as well as the applied angular frequency during loading generally have an impact on the measured phase shift δ. If the origin along the time axis is chosen to coincide with the point of maximum strain, the constitutive equation of the stress and strain functions reads as [40]:

$$\gamma(t) = \gamma_0 \sin(\omega t) \tag{5}$$

$$\tau(t) = \tau_0 \sin(\omega t + \delta) \tag{6}$$

where γ_0 and τ_0 are the amplitude of the shear strain and shear stress, respectively. It is convenient to transfer the stress and strain functions into the frequency domain as their complex quantities using the algebraic operations used in harmonic systems:

$$\gamma^* = \gamma_0 \exp(i\omega t) \tag{7}$$

$$\tau^* = \tau_0 \exp(i(\omega t + \delta)) \tag{8}$$

Based on these harmonic relations, one can define the complex shear modulus G^* and two different dynamic moduli with their quotient:

$$G^* = \frac{\tau^*}{\gamma^*} = \frac{\tau_0}{\gamma_0}\cos(\delta) + i\frac{\tau_0}{\gamma_0}\sin(\delta) \tag{9}$$

$$G' = \frac{\tau_0}{\gamma_0}\cos(\delta) \tag{10}$$

$$G'' = \frac{\tau_0}{\gamma_0}\sin(\delta) \tag{11}$$

$$\tan(\delta) = \frac{G''}{G'} \tag{12}$$

The shear storage modulus G' describes the mechanical energy stored by the material during a loading cycle which represents the reversible part of the dynamic mechanical material behaviour after a load cycle. The loss modulus G'' accounts for the ability to dissipate the mechanical energy through internal molecular motions. The damping factor $\tan(\delta)$ represents the ratio of the viscous and the elastic portion of the viscoelastic deformation behaviour.

The following sections provide an overview of the various oscillatory tests with controlled shear strain that were conducted utilising this complex mathematical form to measure and predict the viscoelastic properties and chemical shrinkage of the photopolymer.

2.4. Methods

2.4.1. UV rheometry

The UV rheometry measurement permits the monitoring of the evolution of the viscoelastic properties in the gel-sol transition of the photopolymer resin. Figure 2 shows a schematic representation of the experimental procedure and the UV curing progress of the liquid resin sandwiched between the parallel-plate measuring system consisting of a transparent bottom plate made of quartz glass.

The investigation of the evolution of the viscoelastic properties and the chemical shrinkage of PR48 resin during the UV curing was carried out with the hybrid rheometer Discovery HR-3 (TA Instruments, New Castle, DE, USA) upgraded with the OmniCure® S2000 UV light source (Excelitas, Waltham, MA, USA). A parallel plate measuring system consisting of a quartz plate and a disposable aluminium top plate with a diameter of 20 mm was used.

The measurement gap was adjusted to 500 µm. The measurement gap of $d_{gap} = 500$ µm was determined through preliminary tests performed to determine appropriate experimental test parameters. The PR48 photopolymer resin cures rapidly even at low UV light intensity and room temperature,

and hardens into a very stiff substance. Therefore, when a thinner layer of photopolymer was used between two parallel plates, the cured solid polymer prevented oscillation through the top plate. As a result, the maximum allowable torque specified for the test instrument was reached and the test stopped. In such a short period of time, it is not feasible to monitor the change in the viscoelastic properties and decrease in the measurement gap for the chemical shrinkage of the material during UV curing. This selected thickness corresponds to approximately 5 to 10 times the typical layer thickness provided by conventional SLA and DLP 3D printers used to print photopolymer parts [2]. As mentioned in Section 5 later, the agreement between the maximum shrinkage determined by UV rheometer tests and determined by density measurements in static mode [37] indicates that the transverse shrinkage of the polymer is negligible at this layer thickness.

The UV light intensity was adjusted to $\mathcal{I}_0 = 10.12$ mW/cm^2 at the top surface of the quartz plate for all tests. For each selected isothermal test, the temperature of the upper aluminium plate was set to the desired temperature before the photopolymer resin was applied onto the quartz plate. For the measurement gap of 500 µm, a liquid photopolymer sample volume of approximately 157 µL was carefully injected with a pipette onto the quartz glass plate. An isothermal step was applied at the test temperature for 10 minutes for stabilization at each measurement point.

The measurement of the rheological properties were performed in the auto-strain mode with an initial strain of $\gamma_0 = 0.1\%$. The auto-strain feature was programmed to automatically adjust the strain amplitude to material changes in the linear viscoelastic region of the least cured solid sample ($q = 0.63$) in Section 4.1. To avoid the breaking of the polymer network, the strain amplitude increased to the maximum allowable value at the beginning of the curing and then decreased with progressing crosslinking when gelation starts. In other words, auto-strain adjustment was used to improve signal quality throughout a single experiment, as the optimal measurement conditions for a liquid material are not the same as those for a rigid solid. The adjustment amplitude range was selected from $\gamma_0 = 0.01\%$ to 1% according to the amplitude sweep tests. The normal force is set to 0 ± 0.1 N to minimize the effect of the excessive tensile stresses generated by chemical shrinkage.

2.4.2. Dynamic mechanical analysis

Dynamic mechanical analysis (DMA) is a conventional measurement technique in which the elastic and viscous responses of the polymer materials

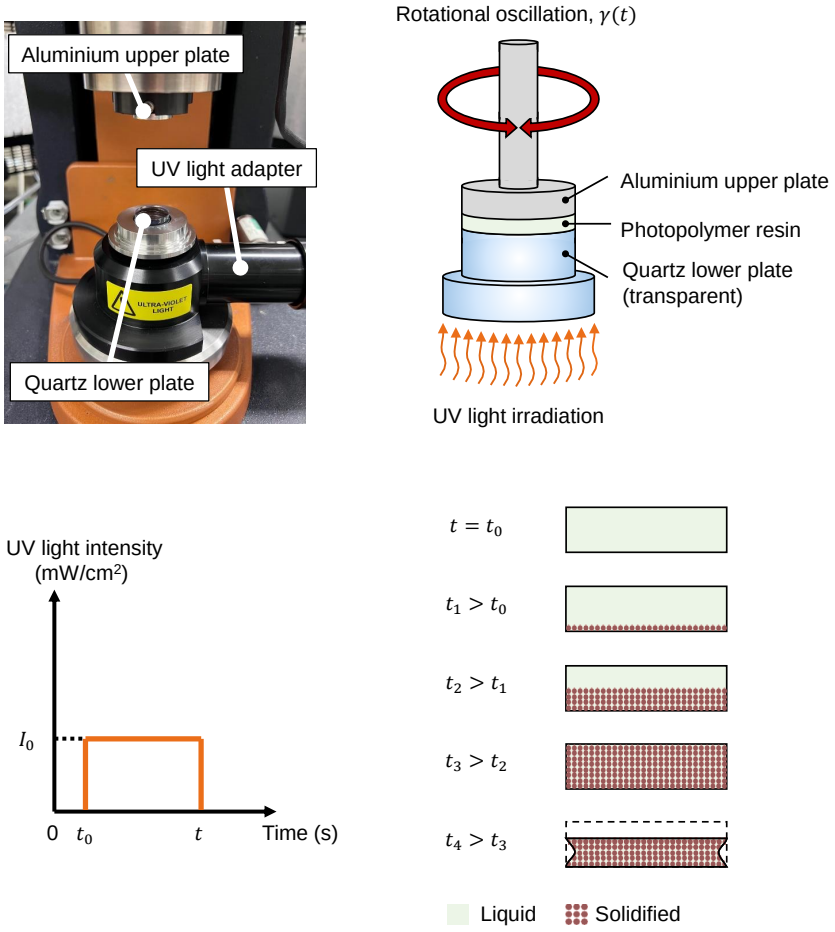

Figure 2: Outline of the UV rheometry experiment. Top left: Experimental setup of the Discovery HR-3 rheometer with the parallel plates. Top right: Schematic representation of the experimental setup under the oscillatory conditions and UV irradiation. Bottom left: Irradiation of constant UV light over time during the crosslinking process. Bottom right: Schematic representation of the curing process in the liquid photopolymer between the parallel plates during the UV irradiation.

subjected to a sinusoidal oscillatory force are monitored over temperature, time, frequency or amplitude sweeps.

In this work, DMA was employed to study the viscoelastic behaviour of the solid PR48 photopolymer samples in torsion mode. Amplitude, temperature and frequency sweep tests were run on a modular rheometer MCR502 (Anton Paar, Graz, Austria) with an integrated environmental chamber CTD

600 (by Anton Paar) which was used with air and nitrogen. A solid rectangular fixture system SRF5 (by Anton Paar) was used for all the experiments in this section with force-controlled measurements. A normal force of 1 N was applied in tension mode to prevent the specimens from buckling or excessive tensile forces due to thermal expansion and contraction when the material is tested over a wide temperature range. The top of the specimen was subjected to a controlled shear strain given in Equation 5 while the bottom is fixed as outlined in Figure 3.

Rectangular photopolymer samples were prepared by injecting the liquid resin between two glass slides separated by Teflon molds in order to cure in the UV chamber named UVP Crosslinker CL-1000L (Analytik Jena AG, Jena, Germany). According to the standard ISO 6721-2 [41], specimens with the dimensions of $50 \times 10 \times 1$ mm^3 (length $\times$ width $\times$ thickness) were manufactured by exposing them to UV light for 3, 8, 30 and 540 min.

Moreover, before DMA testing, the samples were analysed at least 3 times in a DSC to determine the average degree of cure listed in Table 1 using Equation 4.

Table 1: Degree of cure q of the samples for the DMA measurements based on the light exposure time t_{exp}.

t_{exp} **[mins]**	3	8	30	540
q **[-]**	0.63	0.89	0.92	0.96

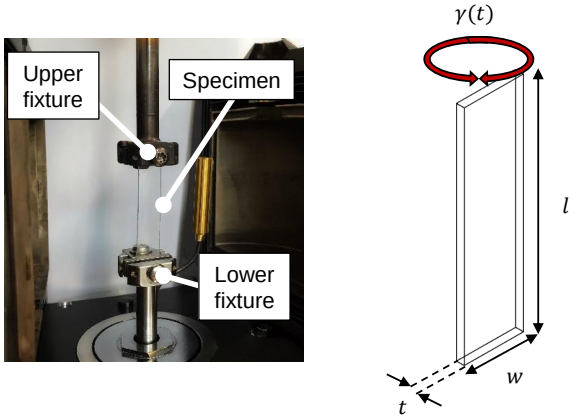

Figure 3: Outline of the DMA experiments in torsional mode. Left: Specimen mounted in Anton Paar MCR 502 rheometer where the shear excitation is applied to the top of the specimen by the upper mobile fixture. Right: Schematic of rectangular sample with dimensions of $50 \times 10 \times 1$ mm^3 ($l \times w \times t$) used in DMA tests according to ISO 6721-2 standards.

3. Evolution of the viscoelastic properties during the UV curing reaction

3.1. Time sweep tests

Time sweep tests for 400 s were performed at different constant frequencies ($f = 0.1, 1, 10, 100$ Hz) at constant UV intensity and at several isothermal conditions ($\theta = 10, 20, 30, 40, 50, 60$ °C). The onset time of UV light exposure was set to 60 s for all tests.

The direct experimental results of the change in the storage modulus G' for all measurements are provided in Appendix B. As shown in the schematic representations in Figure 2, initially, the photopolymer resin is conditioned with sinusoidal shear excitation given by Equation 5 at constant frequency $f = \omega/2\pi$, constant strain amplitude γ_0, and isothermal condition θ for up to $t_0 = 60$ s ($0 < t < t_0$). Then, UV light is activated unidirectionally from the bottom of the quartz plate upwards ($t = t_0$). Furthermore, curing starts at the bottom of the photopolymer layer ($t = t_1$) and then progresses in the vertical direction ($t_1 < t < t_2$). When the solidifying photopolymer layer reaches to the aluminium top plate ($t = t_3$), the rheometer begins to measure the changes in the viscoelastic material properties. Since the curing front takes some time to reach the top plate where the measurement is performed,

a short delay is noticed in the $G' - t$ plot, between the activation of the UV light and the onset of the rise of the shear storage modulus. Therefore, it is necessary to shift all the curves presented in Appendix B such that the storage modulus of G' starts to increase, i.e. the curing starts at $t = 0$ as shown in Figure 4.

The experimental findings of the change in the shear storage modulus G' for frequency values in four different orders of magnitude and at six different isothermal conditions are depicted in Figure 4. All measurements show a rapid increase in the presence of UV light irradiation, in addition to different evolutions of the shear storage moduli due to frequency-dependent material behaviour. The shear storage modulus of the progressively cured sample reaches its plateau value more rapidly as the frequency value increases. It can be seen that the value of the maximum shear storage modulus obtained is higher than the tests performed at lower frequency. This can be explained by the faster curing of the sample due to lower viscosity as the frequency increases. Consequently, achieving a higher degree of cure due to the lower viscosity also leads to a higher storage modulus at the end of the test. In the literature, this relationship between low viscosity and high degree of cure has also been observed for dual-cured resin cement [42]. As the degree of cure or curing time increases, the difference between the curves belonging to different frequencies in the semi-logarithmic representation decreases.

The constant temperature applied to the photopolymer in the tests leads to two opposing mechanisms. In the first case, higher temperature increases the rate of crosslinking of the photopolymer and allows for a higher degree of cure at the end of the chemical reaction. As a consequence, the photopolymer sample reaches a higher shear storage modulus at the end of the test. In the second case, higher temperature causes a lower shear storage modulus and thus the photopolymer sample becomes softer. These two mechanically and chemically coupled mechanisms occur concurrently and cannot be distinguished in UV rheometer experiments. As shown in Figure 4, in the tests performed at temperatures between 10 °C and 40 °C, the increase in temperature accelerates the curing reaction, resulting in the shear storage modulus to reach its plateau value earlier. However, the temperature-induced acceleration of curing is not comparable in the experiments performed at temperatures between 40 °C and 60 °C. At the end of the tests carried out at $\theta = 50$ °C and 60 °C, it was observed that the samples obtained at the end of the curing reaction were soft, especially in the tests carried out at $f = 0.1$ Hz, and therefore the bottom quartz glass and top aluminium plates could be

easily separated.

3.2. Gelation point

The degree of cure at the gelation point q_{gel} is required for the application of the time-cure superposition principle in the description of viscoelastic properties during the entire UV curing reaction. Therefore, it is necessary to calculate the evolution of the degree of cure given in Equation 2 as a function of temperature, UV light, and time during the UV rheometer test.

We further consider that the UV light intensity decreases exponentially with the layer thickness as it passes through the liquid photopolymer medium, according to the Beer-Lambert law described by the following equation [20]:

$$\mathcal{I}(z) = \exp\left(-\frac{z}{D_p}\right)\mathcal{I}_0 \tag{13}$$

where $\mathcal{I}(z)$ is the light intensity as a function of distance z, D_p denotes the penetration depth, which was determined to be $D_p = 223.2$ µm in the previous study in which the UV curing properties of the PR48 photopolymer resin were examined in detail [37] and $\mathcal{I}_0 = 10.12$ mJ/cm^2 is the UV light intensity on the quartz glass plate. The average value of UV light intensity $\mathcal{I}_{av}$ between parallel plates was used to calculate the effective degree of cure. Using Equation 13, the following mean value is computed:

$$\mathcal{I}_{av} = \frac{1}{d_{gap}}\int_0^{d_{gap}} \mathcal{I}(z)dz \tag{14}$$

The average light intensity was calculated as $\mathcal{I}_{av} = 4.04$ mW/cm^2. This value is close to $\mathcal{I} = 5$ mW/cm^2 which is one of the two UV light intensity values in which the photocalorimetric tests were performed in the previous work [37]. The evolution of the degree of cure during UV rheometer tests was estimated using Equations 2 and 3 and the corresponding maximum attainable degree of cure $q_{\max}$. Figure 5 depicts the evolution of the effective degree of cure for the UV rheometer measurements.

The gelation point is defined as the transition point of a crosslinking polymer from a liquid to a solid [43]. There are two commonly used methods for estimating the gelation point of the photopolymer layer.

According to ASTM standard D4473 [44], the gelation point (t_{gel}) is defined as the point at the intersection of the curves of G' and G'' versus time t ($G' = G''$). This state shows the borderline of a crosslinking polymer liquid

transforming into a solid [45]. This point can be determined by the oscillatory tests performed in the linear viscoelastic range during the crosslinking reaction. In the ASTM standard D4773, the frequency to evaluate the curing behaviour of thermosets is recommended to be set to $f < 1.5$ Hz. In accordance with this standard, the evolution of the viscoelastic properties (G', G'') at $f = 1$ Hz and $\theta = 20$ °C are plotted in Figure 5. It can be seen from the plot that as the sample passes gelation point, both storage and loss moduli start to increase until the maximum attainable degree of cure is reached. From the zoomed window in the same figure, it can be seen that the gelation point (t_{gel}) of the PR48 was reached at $t = 7.93$ s after starting the UV irradiation. The UV energy dose reached at this point is $E_{gel} = 32.04$ mJ/cm^2. The degree of cure at the gelation point was calculated as $q_{gel} = 0.32$ using the model equation of the degree of cure with the test parameters.

The second method utilizes the working curve model developed by Jacobs [46]. According to this model, the relationship between the applied UV light exposure dose $E = \mathcal{I} \times t$ and the resulting cured depth C_d of the photopolymer layer is defined by deriving from the Beer-Lambert law (Equation 13) as follows:

$$C_d = D_p \ln\left(\frac{E}{E_c}\right) \tag{15}$$

Here, the critical exposure energy E_c represents the amount of UV light exposure dose required to solidify the photopolymer at the gelation point. $E_c = 30.63$ mJ/cm^2. The experimental procedure and methodology for determination of the critical exposure energy doses were detailed in the previous article [37]. As a consequence, this yields the time point at $t_{gel} = 7.58$ s which gives almost the same gelation point q_{gel} as the first approach.

3.3. Time-cure superposition

The experimental results of the storage modulus in the time domain were combined with the model equations for the degree of cure. The evolution of the degree of cure during the UV rheometer test was calculated using Equations 2 and 3 for the specified temperature and UV light intensity conditions. This coupling yields several subcurves of the shear storage modulus in the frequency domain depending on the degree of cure, as shown in Figure 6. In this graph, it can be seen that as the temperature increases, two conflicting phenomena occur, similar to those observed in Figure 4 for the photopolymer sample. The increase in temperature leads to an acceleration of the crosslinking process of the photopolymer, resulting in a higher degree of cure in the

same period of time. In this case, the photopolymer is expected to reach a higher shear storage modulus at the end of the higher temperature measurement. It is important to note, however, that increasing temperature also cause another phenomenon. As the temperature rises, the kinetic energy of the polymer increases, leading to an increase in the mobility of the polymer chains. This increased mobility of polymer chains results in a decrease in the storage modulus. As a result, in the subcurves presented for $t = 0 - 250$ s, the curves of storage modulus fall within the same range after a certain time due to these opposite phenomena. Master curves were created by manually shifting these subcurves in the first 50 seconds of these measurements to perform time-cure superposition similar to the work of Adolf and Martin [47] and Eom et al. [48].

The shift factor exponents to the base 10 s_q calculated for the measurements performed at different isothermal conditions are presented in Figure 7. The shift factors are almost independent of temperature up to $q = 0.52$ in spite of a spread of values. Eom et al. [48] identified the gelation point at this value which is not the case here, as the gelation point was identified previously at $q_{gel} = 0.32$. This difference can be explained by the nonlinear effect on the evolution of the shift factors as the degree of cure approaches its maximum value $q_{\max}(\mathcal{I}, \theta)$. In future studies, this point can be rheologically investigated in order to perform a general and valid material modelling that takes into account the effect of temperature and $q_{\max}(\mathcal{I}, \theta)$ during UV curing.

In the next step, experimental results at $\theta = 20$ °C were selected as an ideal case to model the degree of cure- and temperature-dependent viscoelastic properties of the material by combining the DMA and UV rheometer measurements. Since the lowest degree of cure tested in DMA in Section 2.4.2 was $q = 0.63$ which corresponds to the first 40 seconds of the measurement, a master curve was built from curves up to this value at $q_{ref} = 0.53$ and given in Figure 8. This master curve shows that as the degree of cure and frequency increase, the shear storage modulus also increases.

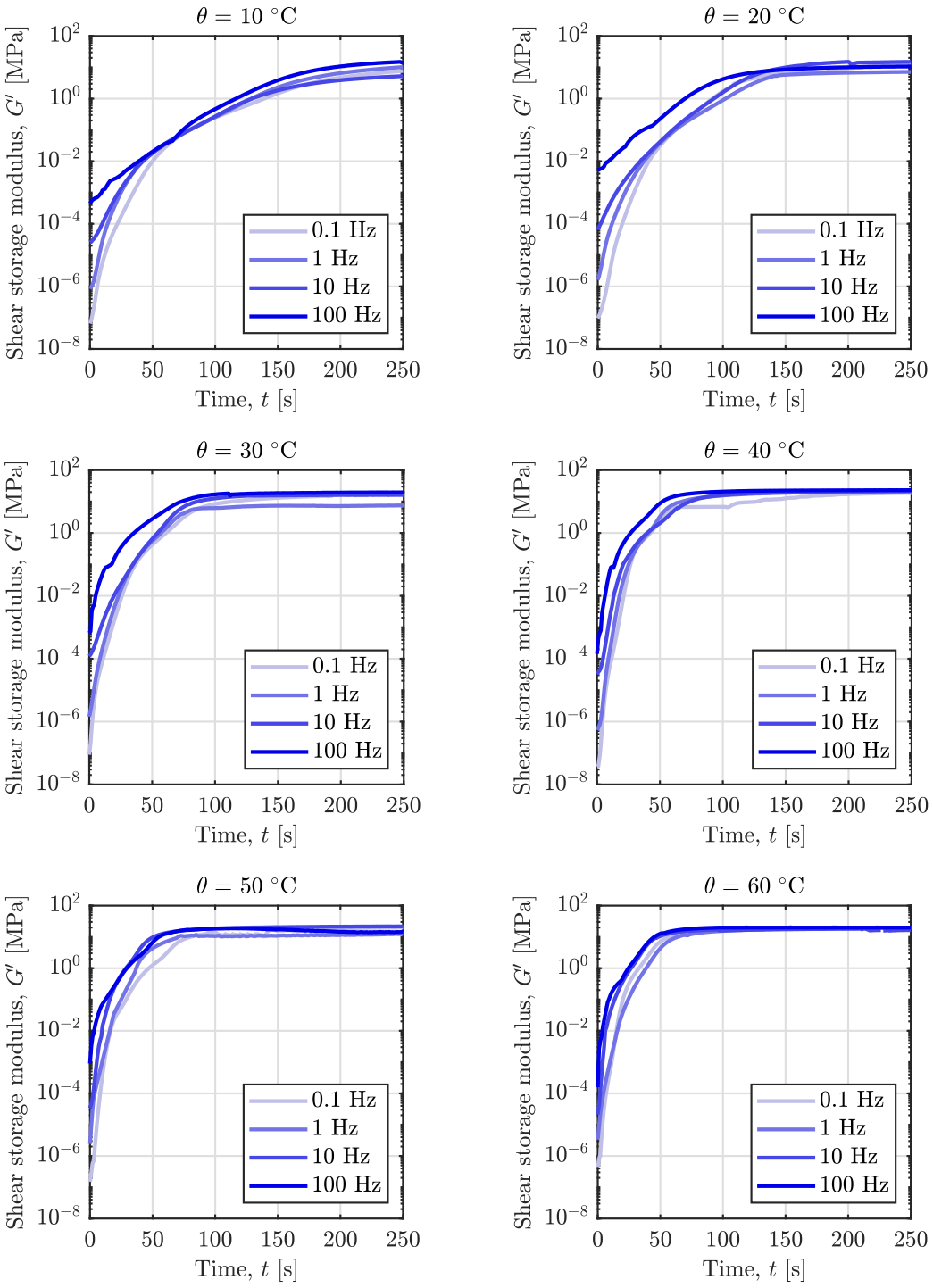

Figure 4: Evolution of the shear storage modulus G' with progressing crosslinking in the photopolymer layer at different isothermal conditions and frequencies (plotted for $t = 0 - 250$ s for better visualization).

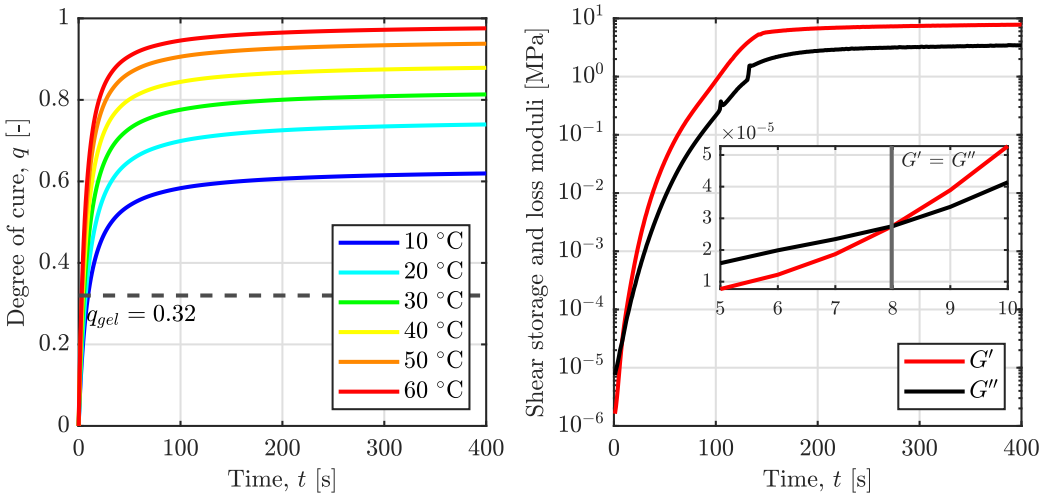

Figure 5: Left: Evolution of the degree of cure q in the UV rheometry measurements during the crosslinking calculated by Equations 2 and 3 with the identified parameters given in Tables A.8 and A.9. Right: Determination of time instant of the gelation point where $G' = G''$ equilibrium is satisfied according the ASTM D4473.

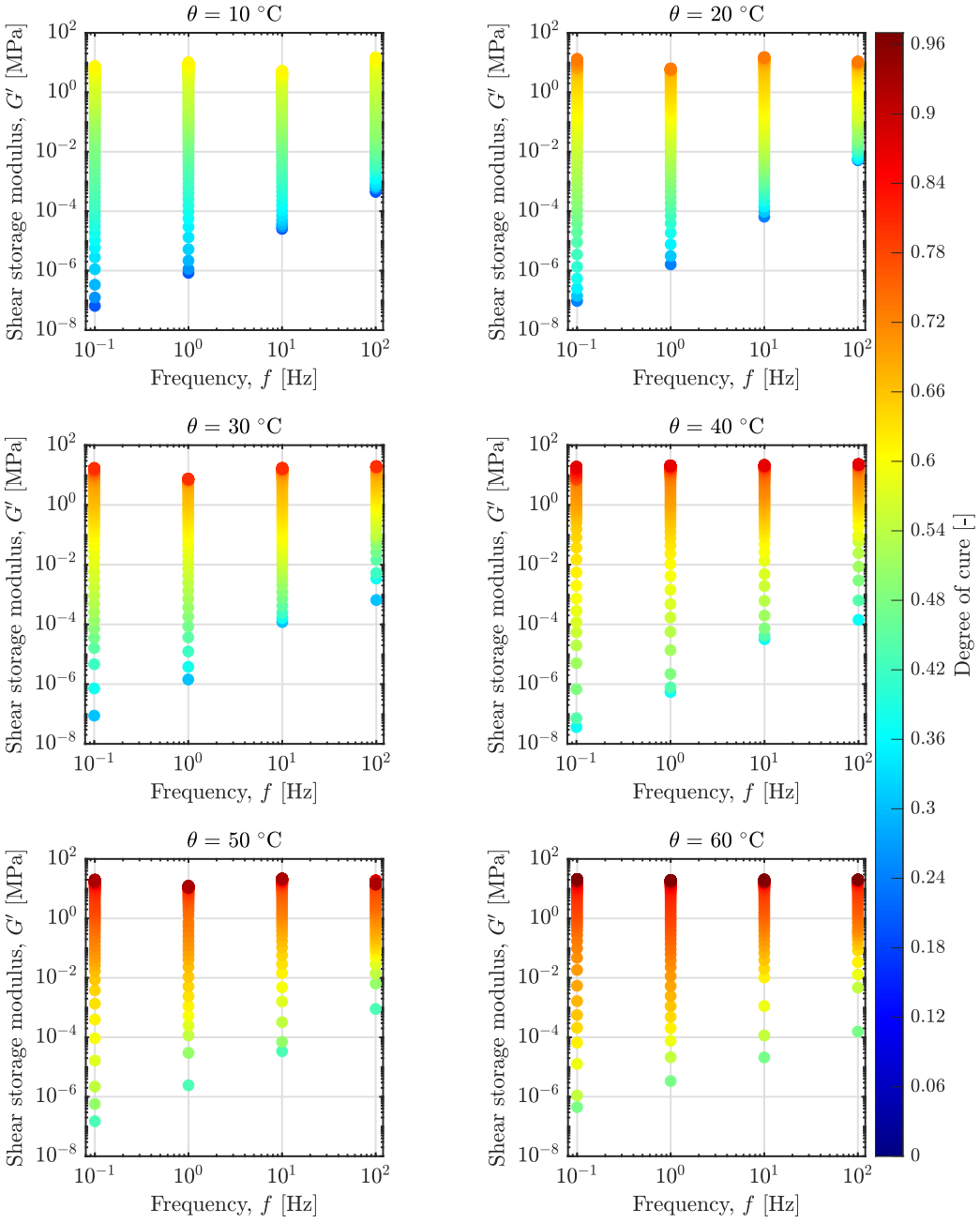

Figure 6: Transformation of the curves of the shear storage modulus in Figure 4 into the frequency domain using the model equation of the degree of cure at various constant degree of cure (plotted for $t = 0 - 250$ s).

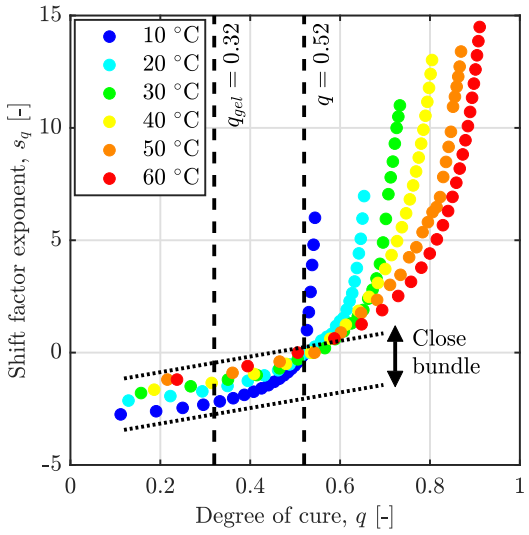

Figure 7: Shift factor exponents to the base 10, $s_q(q)$, as a function of degree of cure q obtained by manual shifting at $q_{ref} = 0.53$ to build the master curves based on the UV rheometer measurements in the first 50 seconds.

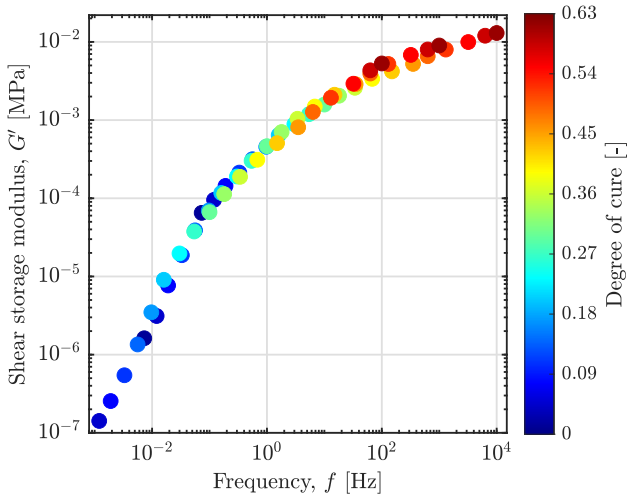

Figure 8: Resulting master curve after shifting the subcurves of Figure 6 at $\theta = 20$ °C at $q_{ref} = 0.53$ for the first 40 seconds (time point corresponding to $q = 0.63$).

4. Evolution of the viscoelastic properties after the UV curing reaction

4.1. Amplitude sweep tests

In this study, the preset of a strain sweep (also called shear strain amplitude sweep) was chosen with a controlled shear strain $\gamma_0(t) = \gamma_0 \sin(\omega t)$ with a constant angular frequency $\omega = 2\pi f$ and a variable strain amplitude increasing with time $\gamma_0 = \gamma_0(t)$. Strain amplitude tests ranging from 0.01% to 10% were carried out for specimens with 4 different degrees of cure at a constant temperature of $\theta = 20$ °C and a frequency of $f = 1$ Hz. For data acquisition, five data points per decade were distributed evenly using a logarithmic rule. The tolerance range of deviation for G' and G'' was selected $\pm 10\%$ around the plateau value according to ASTM D7175 and DIN 51810-2 [49, 50]. In other words, all the dynamic moduli values less than 90% of the plateau value were assessed to be outside the linear viscoelastic region.

The experimental results of specimens cured at different levels are displayed in Figure 9. The damping factors are provided in Appendix C.1. This plot indicates that the storage and loss moduli are independent of the applied strain amplitude under cyclic loading at small strains for all specimens. Furthermore, as the degree of cure increases, the plateau values increase for the storage moduli. This difference in moduli is that higher crosslinked material tends to be harder and stiffer. The storage and loss moduli values remained within the tolerance value of $\pm 10\%$ provided in the test standards, up to the strain values of $\gamma_0 = 1.586\%$ for $q = 0.63, 0.89, 0.92$ and $\gamma_0 = 1\%$ for $q = 0.96$. A nonlinear effect occurs when strains exceed these limiting values, and the dynamic material properties become strain dependent. When cured, the PR48 resin becomes a hard and brittle material and presents a brittle fracturing at strain values greater than $\gamma_0 = 1.586\%$. The plateau values and limiting strain values of the storage and loss moduli in the linear viscoelastic region are summarized in Table 2. The optimal amplitude should be chosen smaller than the limiting value ($\gamma_{0_{lim}} = 1\%$) in order to carry out the measurements in the linear regime. A value of $\gamma_0 = 0.1\%$ was chosen for the temperature and frequency sweep tests in the following sections to prevent the formation of micro- and macro-cracks throughout the test since the material is hard and brittle.

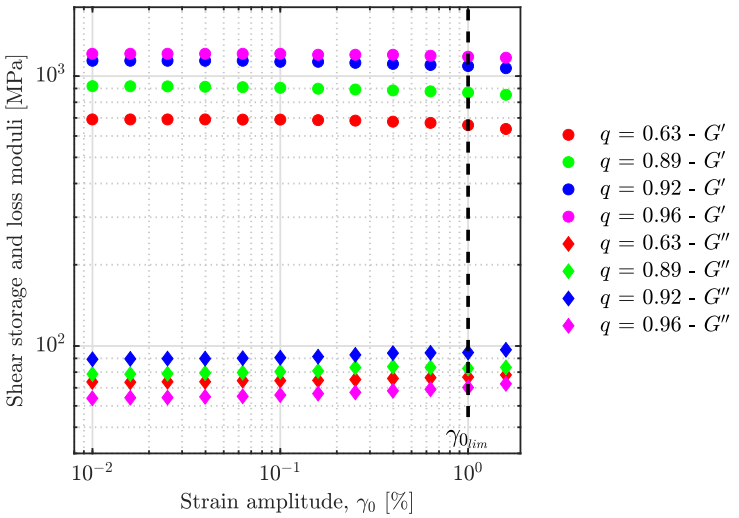

Figure 9: Storage and loss moduli as a function of strain amplitude at $f = 1$ Hz and $\theta = 20$ °C for the samples with $q = 0.63, 0.89, 0.92, 0.96$.

Table 2: Dynamic material properties and limiting value $\gamma_{0_{lim}}$ of linear viscoelastic region obtained as a result of strain scanning of samples with different degrees of cure q.

q [-]	G' [MPa]	G'' [MPa]	$\gamma_{0_{lim}}$ [%]
0.63	679.914 ± 22.238	74.982 ± 1.538	1.586
0.89	896.172 ± 11.356	81.064 ± 2.783	1.586
0.92	1120.283 ± 17.117	91.915 ± 2.616	1.586
0.96	1204.327 ± 9.773	66.331 ± 2.353	1.001

4.2. Temperature sweep tests

Temperature sweep tests were conducted in the temperature range from −110 °C to 160 °C for samples with different curing states. At the start of the experiment, the test chamber was cooled down to −110 °C by applying a 20-minute isotherm to ensure the temperature stability of the sample. Then, the experiments were run at a heating ramp of 1 °C/min, with a constant frequency of $f = 1$ Hz and a strain amplitude of $\gamma_0 = 0.1\%$. The viscoelastic material properties were measured at a data point step every 0.5 °C.

Figure 10 depicts the evolution of the shear storage modulus and the damping factor, G' and $\tan(\delta)$, as a function of temperature for samples at

various cured states. The distribution of the storage modulus is increasing with increasing degree of cure, if $\theta > -40$ °C. This plot also demonstrates that the glass transition occurs at a wide range of temperatures, from about -40 °C to 140 °C. This temperature range has been chosen as the range of interest for the frequency sweep tests given in the Section 4.3.

Furthermore, an increase in the shear storage moduli of the samples with $q = 0.63$ and 0.89 was observed after 140 °C. This increase is due to thermal curing of free monomers.

All samples undergo a thermal transition before -90 °C and after 60 °C in the glassy state, denoted as β- and α-transition, respectively. The β-transition temperatures are around $\theta_\beta = -92$ °C, as listed in Table 3. On the one hand, it can be stated that the β-transition temperature θ_β is almost independent of the degree of cure q within the curing range of tested specimens in the DMA. On the other hand, the glass transition temperature is strongly dependent on the curing and rises with the degree of cure, see Table 3.

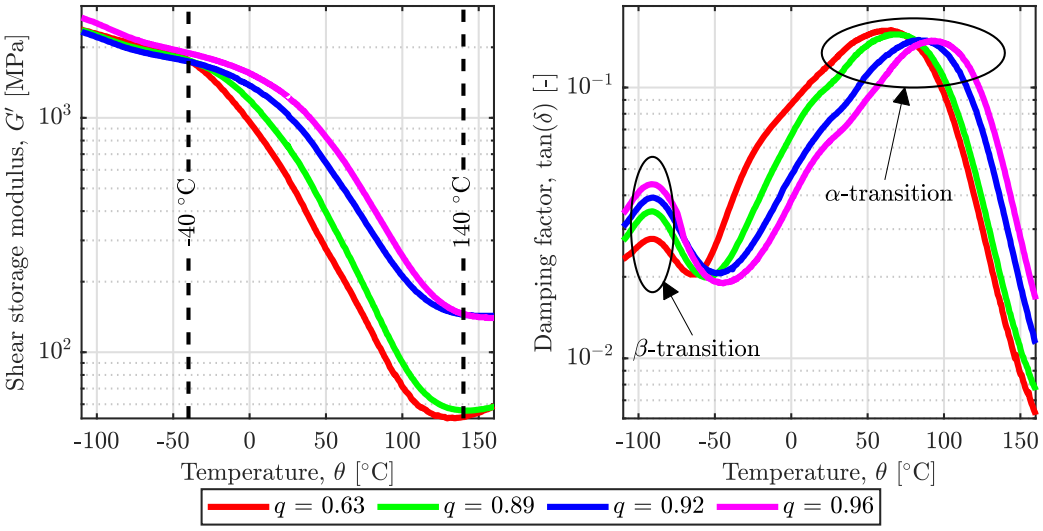

Figure 10: DMA thermograms of the cured polymers. Left: storage loss moduli, right: damping factors as a function of temperature at $f = 1$ Hz and $\gamma = 0.1\%$ at a heating rate of 1 °C/min for the samples cured at different levels.

4.3. Frequency sweep tests

Frequency sweep tests were carried out for materials in different curing states for isothermal conditions ranging from -40 °C to 140 °C at certain

Table 3: Thermal transition temperatures for the samples cured at different levels (θ_β: β-relaxation temperature, θ_α: glass transition (α-relaxation) temperature).

Degree of cure, q [-]	θ_β **[°C]**	θ_α **[°C]**
0.63	−92.4	68.9
0.89	−91.4	73.1
0.92	−91.4	83.4
0.96	−91.4	92.5

intervals. As the slopes of the dynamic moduli are expected to be more pronounced in this temperature range as presented in Figure 10 as a consequence of the temperature sweep tests, a 10 °C temperature step was selected to have better resolution in the range of the thermal transitions. For each isothermal frequency sweep test, a 10-minute isothermal step was performed to ensure temperature stabilization of the sample before performing the dynamic test. The frequency scanning range was 0.01 to 10 Hz, with five measuring points each decade equally distributed on a logarithmic scale. The applied strain amplitude was $\gamma_0 = 0.1\%$ for all samples as specified in Section 4.1.

The corresponding results of the shear storage modulus G' measured from isothermal frequency sweeps are shown in Figure 11 for four samples at different curing condition. The shear loss modulus G'' isothermal curves as a function of frequency for all samples are given in Appendix C.2. It can be observed that the highly cured samples at low temperatures show almost the same value of G'. It can be concluded that further lowering the temperature for less cured samples leads to the same plateau value of the storage modulus in the glassy case where we have frequency independent material properties in the high frequency region ($G' \approx 2000$ MPa). The storage modulus begins to decrease as the temperature rises. At higher temperatures, the shear storage modulus decreases faster as the degree of cure decreases. Furthermore, the equilibrium modulus at the highest test temperature reduces with decreasing degree of cure ($\theta_{\max} = 140$ °C). In addition, the storage modulus increases after 120 °C for the sample with $q = 0.63$ and after 130 °C for the sample with $q = 0.89$, indicating thermal curing, as we observed after 140 °C in the temperature sweep test reported in Section 4.2. This is because samples are likely to begin thermally curing at lower temperatures, provided they have had sufficient time to reach the activation energy required for molecular

mobility during isothermal measurements.

The Cole-Cole diagram enables to determine whether a material has a thermorheologically simple behaviour in order to construct its master curve by applying the time-temperature superposition principle (TTSP) on the frequency sweep test results performed at a certain temperature range [51]. Figure 12 shows Cole-Cole curves for four different samples. Cole-Cole diagrams appear continuous and smooth for all experimental data and show that cured PR48 samples are thermorheologically simple in the temperature range studied.

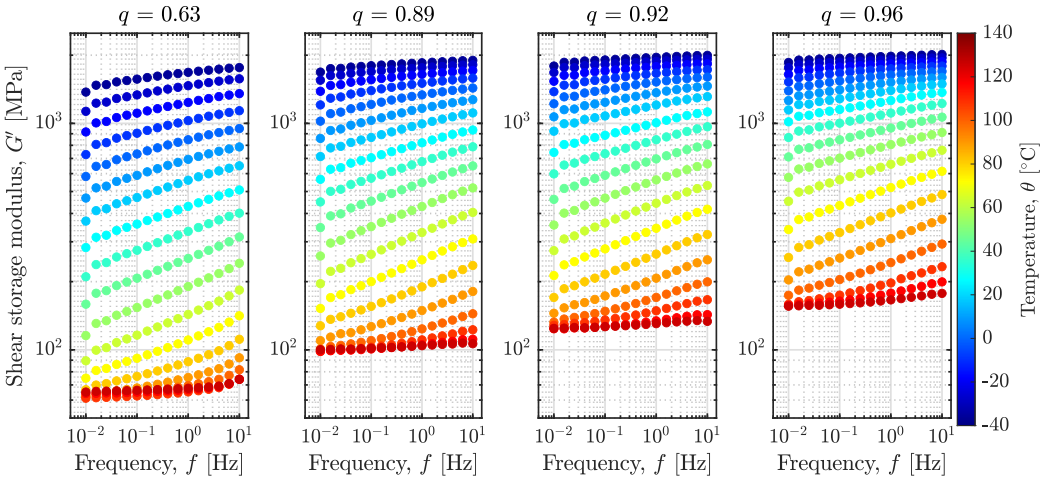

Figure 11: Isothermal frequency sweep curves of the shear storage modulus G' obtained from the DMA tests of the samples with different degrees of cure $q = 0.63, 0.89, 0.92, 0.96$.

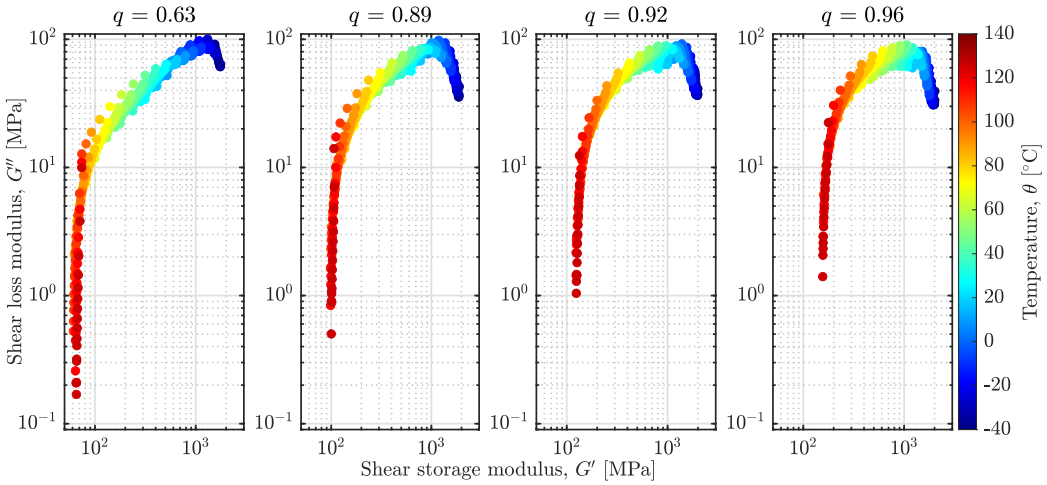

Figure 12: Cole-Cole curves (shear storage modulus G' vs. shear loss modulus G'') of the samples at different curing states. The measurement results were obtained through frequency sweep tests ($f = 0.01 - 10$ Hz) performed at isothermal conditions between -40 °C and 140 °C.

4.4. Time-temperature superposition

The time-temperature superposition principle (TTSP) was applied to the experimental measurements of the frequency sweep tests in order to achieve viscoelastic material characteristics over a broader frequency range. This application allowed for the construction of the master curve using mere horizontal shifts in the experimental data. For each sample with varying degree of cure, isothermal curves at $\theta_{ref} = 20$ °C were used as the reference for the generation of the master curves.

According to the TTSP, frequency sweep curves at lower temperatures were shifted to higher frequencies and vice versa. The resultant master curves of all samples at a reference temperature of $\theta_{ref} = 20$ °C are presented in Figure C.20.

Figure 13 shows the corresponding exponents to the base 10 of the shift factors for constructing the master curves at the reference temperature $\theta_{ref} = 20$ °C applying the TTSP. It should be emphasized that no explicit dependence on the degree of cure up to 90 °C was observed. The reason for the slight difference after 90 °C may result from the test temperature exceeding the glass transition temperature θ_α of the samples obtained by the temperature sweep tests in Section 4.2. Generally speaking, considering the Cole-Cole curve in Figure 12 and a temperature range chosen away from the

onset temperature of thermal curing ($\theta_{onset} = 120$ °C according to isothermal frequency sweep experiments), these shift factors can be described with a single equation based solely on temperature. This key aspect will enable the time-temperature superposition principle to be represented independently of the time-cure superposition principle in Section 4.6. As a result, the WLF equation was concurrently adapted for all four independent datasets of shift factors at each reference temperature as follows:

$$s_\theta(\theta) = \frac{-C_1\,(\theta - \theta_{ref})}{C_2 + (\theta - \theta_{ref})} \tag{16}$$

where θ is the temperature of interest, θ_{ref} is the reference temperature chosen to construct the master curve and C_1 and C_2 are the material constants.

The WLF parameters identified are $C_1 = 81.42$ and $C_2 = 595.8$ °C at $\theta_{ref} = 20$ °C. The fitting curve obtained using the WLF equation to the temperature-dependent shift factors calculated at $\theta_{ref} = 20$ °C is depicted in Figure 13.

Figure C.20 also shows the master curves that were constructed by shifting isothermal curves given in Figure 11 with the shift factors obtained from the WLF equation. These curves obtained by the WLF equation were employed in the material modelling in the next sections to consider the independence from degree of cure.

4.5. Identification of relaxation times and stiffnesses at the reference point

In this work, a degree of cure- and temperature-dependent generalized Maxwell model is proposed to represent the measurement results given in Section 4.4 for the time-cure superposition to be performed in the next section. A schematic representation of a generalized Maxwell model with n elements as a part of the rheological network is depicted in Figure C.21.

Depending on the temperature and the degree of cure, the shear storage G' and the shear loss modulus G'' are defined as:

$$G'\left(\omega, G_i, \lambda_i\right) = G_\infty(q) + \sum_{i=1}^{n} G_i \frac{\left(\omega\lambda_i(\theta, q)\right)^2}{1 + \left(\omega\lambda_i(\theta, q)\right)^2} \tag{17}$$

$$G''\left(\omega, G_i, \lambda_i\right) = \sum_{i=1}^{n} G_i \frac{\omega\lambda_i(\theta, q)}{1 + \left(\omega\lambda_i(\theta, q)\right)^2} \tag{18}$$

where G_∞ is degree of cure-dependent equilibrium stiffness, λ_i are degree of cure- and temperature-dependent relaxation times, and G_i are constant

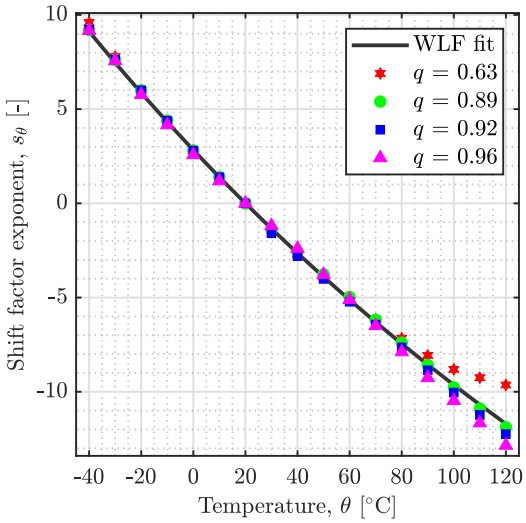

Figure 13: Shift factor exponents to the base 10 of time-temperature superposition at $\theta_{ref} = 20$ °C for samples with different degrees of cure (see Figure C.20) and fitted curve of these factors using the WLF equation.

stiffnesses for any temperature and degree of cure. The stiffnesses G_i and viscosities η_i for each Maxwell element are related to the relaxation time λ_i in such a way that:

$$\lambda_i = \frac{\eta_i}{G_i} \tag{19}$$

The number of Maxwell elements n is chosen as 30. The details of the selection method can be found in Appendix C.4.2.

4.6. Time-cure superposition

To account for changes in viscoelastic properties with temperature and curing, relaxation times λ_i are defined as a function of shift factors determined by time-temperature s_θ and time-cure superposition s_q as follows:

$$\lambda_i(\theta, q) = \lambda_i^{ref} 10^{s_\theta(\theta)+s_q(q)} \tag{20}$$

where λ_i^{ref} indicates the relaxation times determined at the given reference temperature θ_{ref} and degree of cure q_{ref}.

The results are presented in Figure 14. This figure compares the master curves derived from the experimental findings with the curves simulated by identifying $\lambda_i(\theta, q)$ and $G_\infty(q)$. In this comparative graph, on the one

hand, the prediction of material behaviour at high frequencies, i.e. at low temperatures, showed a good agreement with the experimental data. On the other hand, especially for samples with lower degrees of cure, it was observed that the representation of the material behaviour was not sufficient as one goes towards low frequencies, i.e. at high temperatures. These regions, where the model estimation is weak, correspond to the curves obtained in the isothermal frequency sweep tests performed above the glass transition temperature θ_α in Section 4.3. It can be deduced that the proposed model does not provide a suitable estimation after glass transition temperature θ_α and it is recommended not to use the proposed time-cure superposition method in this region. Moreover, the identified equilibrium modulus $G_\infty(q)$ listed in Table 4 also indicate a considerable dependence on the degree of cure q.

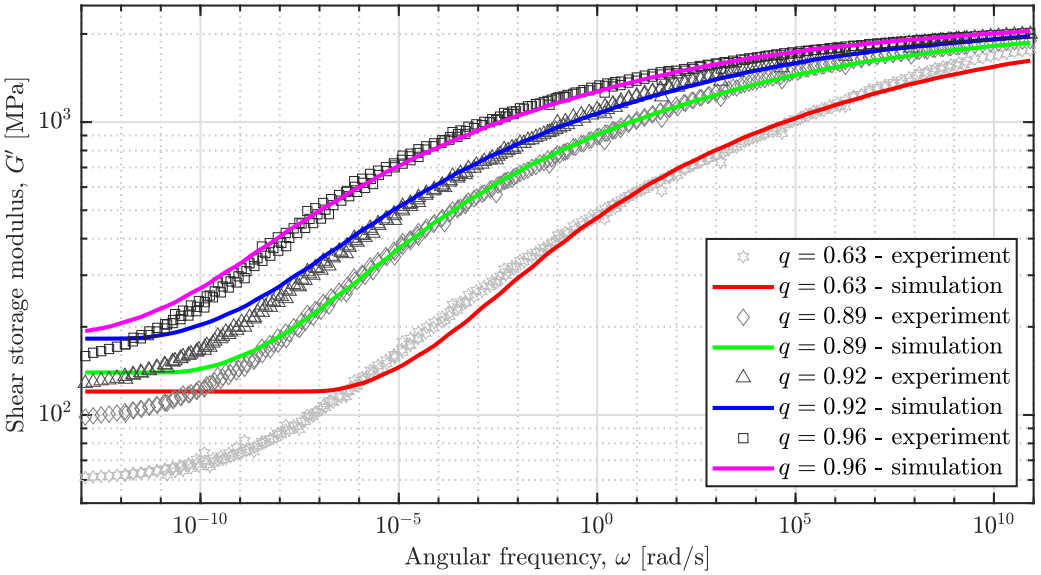

Figure 14: Experimental and simulated master curves at $\theta_{ref} = 20$ °C. After determining the parameters using the generalized Maxwell model at the reference point $q_{ref} = 0.96$ and $\theta_{ref} = 20$ °C, the time-cure superposition was applied to the curves for $q = 0.63, 0.89$ and 0.92 by shifting the relaxation times $\lambda_i(\theta, q)$ with certain shift factors $s_q(q)$ $(s_\theta(\theta_{ref}) = 0)$ using Equation 20 and calculating the equilibrium moduli $G_\infty(q)$ depending on the degree of cure q.

Table 4: Degree of cure-dependent shift factors $s_q(q)$ and equilibrium moduli $G_\infty(q)$ identified according to the reference point $\theta_{ref} = 20$ °C and $q_{ref} = 0.96$.

q **[-]**	$s_q(q)$ **[-]**	G_∞ **[MPa]**
0.63	−6.551	120.248
0.89	−2.850	139.657
0.92	−1.764	182.233
0.96	0	189.754

The equilibrium shear modulus depending on the degree of cure, is represented by the expression presented in [22, 52]:

$$G_\infty = G_{\infty 1} \exp\left(G_{\infty 2}\left(q - q_{gel}\right)\right) + G_{\infty 3} \tag{21}$$

where $G_{\infty 1}$, $G_{\infty 2}$ and $G_{\infty 3}$ are fitting parameters and q_{gel} is the degree of cure at the gelation point ($q_{gel} = 0.32$). The identified fitting parameters are listed in Table 5. As presented in Figure C.24, the comparison of experimental and simulated results for the equilibrium modulus $G_\infty(q)$ reveals a good representation.

Table 5: Identified parameters of the degree of cure-dependent equilibrium modulus $G_\infty(q)$ given in Equation 21

Parameter	$G_{\infty 1}$ **[MPa]**	$G_{\infty 2}$ **[-]**	$G_{\infty 3}$ **[MPa]**	R^2 **[-]**
Value	0.067	11.01	116.9	0.871

4.7. Time-cure superposition for the entire curing process

To describe the evolution of viscoelastic material properties of the photopolymer during the entire crosslinking reaction, the shift factors from UV rheometer measurements can be combined with those from DMA measurements. To achieve this, the shift factors of the UV rheometer tests at $\theta = 20$ °C given in Figure 7 were vertically and equally shifted downwards to build a continuous curve with the shift factors obtained from the DMA measurements (see Appendix D).

Rehbein et al. [23] effectively employed a mathematical formulation to describe the shift factors obtained for the time-cure superposition, drawing inspiration from the earlier work of Eom et al. [48]. In this mathematical

representation, the shift factor is represented as a function of degree of cure q by a linear equation before the gelation point q_{gel}, and then, the dependence of the shift factor on the degree of cure is described by a fitting function as follows:

$$s_q(q) = \begin{cases} s_{q1}\,(q - q_{gel}) + s_{q_{gel}}, & q < q_{gel} \\ s_{q_{gel}} \cdot s_{q2}^{\,q-q_{gel}} \left(\frac{q_{\max}-q}{q_{\max}-q_{gel}}\right)^{s_{q3}}, & q \geq q_{gel} \end{cases} \tag{22}$$

where $s_{q_{gel}}$ is the shift factor at the gelation point of the photopolymer and $s_{q_{gel}}$, s_{q1}, s_{q2}, and s_{q3} are dimensionless model parameters to be identified.

Table 6 lists the identified parameters for the entire curing process defined by Equation 22. Figure 15 displays the fitting results which indicates that this model equation reveals satisfactory agreement with the shift factors experimentally obtained by applying the time-cure superposition.

Table 6: Identified parameters of the time-cure shift functions $s_q(q)$ given in Equation 22.

Parameter	s_{q1}	s_{q2}	s_{q3}	$s_{q_{gel}}$
Value [-]	4.247	1.315	0.696	−10.17

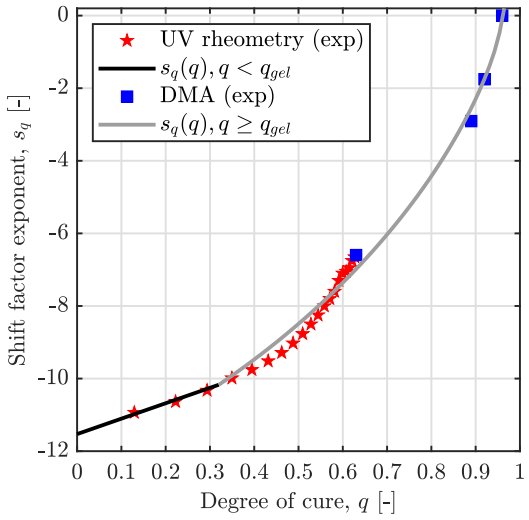

Figure 15: Representation of the time-cure shift factors calculated by the combination of UV rheometer and DMA measurement results and fitting curve obtained by the mathematical representation given in Equation 22.

5. Polymerization shrinkage

To estimate the chemical shrinkage caused by UV curing, the measurement gap change d_{gap} of the photopolymer layer over time was recorded in UV rheometer tests performed in Section 3.1. The temperature values ($\theta = 10, 20, 30, 40, 50, 60$ °C) are sufficiently lower than the onset temperature of thermal curing of the liquid photopolymer ($\theta_{onset} > 165$ °C) determined in the previous study [37]. Therefore, the effect of thermal curing is not involved in this study. The measurement results for $f = 1$ Hz were chosen to prevent dependence on low or high frequency and were motivated by investigations of chemical shrinkage measurement using UV rheometry [53, 54].

Considering the initial layer thickness $d_{gap}(0) = 500$ µm, the linear chemical shrinkage strain in the vertical direction of the liquid photopolymer sample is expressed as:

$$\frac{\Delta L}{L}(t) = \frac{d_{gap}(t) - d_{gap}(0)}{d_{gap}(0)} \tag{23}$$

where the $d_{gap}(t)$ denotes the evolution of layer thickness over time.

The temporal evolution of linear chemical shrinkage is presented on the left in Figure 16. To establish the relationship between curing and chemical shrinkage, the change in chemical shrinkage with degree of cure, already calculated in Section 3.2 using Equations 2 and 3, is given on the right side in Figure 16. The following model equation is proposed to assess the curing-induced chemical shrinkage:

$$\frac{\Delta L}{L}(q, \theta) = \alpha \left(- \exp \left(\frac{q}{\beta(\theta)} \right) - 1 \right) \tag{24}$$

where α is a model parameter and $\beta(\theta)$ is a model function that depends on the temperature θ at which the experiment is performed.

To determine the parameter α and function $\beta(\theta)$ corresponding to 6 different temperatures, the parameters in Equation 24 were identified by the nonlinear least square method using the `lsqnonlin` function embedded in Matlab [55]. The prediction results using the identified parameters in Equation 24 are also depicted in Figure 16 (right). To better address the experimental results, the following equation is suggested for $\beta(\theta)$:

$$\beta(\theta) = \beta_1 \left(\frac{\theta}{\theta_0} \right)^{\beta_2} \tag{25}$$

where β_1 and β_2 are model parameters to be identified and $\theta_0 = 1$ °C is merely utilized to maintain unit consistency. Table 7 contains a list of the identified parameters for Equations 24 and 25 (see Appendix E for the details of the fitting method for $\beta(\theta)$ function).

The experimental evolution and estimation of the shrinkage value are shown in Figure 16. The shrinkage progresses depending on the degree of cure until the maximum shrinkage at each temperature is reached during the UV rheometer test. It can be seen that the approximation using this exponential function can estimate the evolution of the chemical shrinkage as a function of the degree of cure and temperature. Furthermore, the maximum shrinkage value was observed at the highest experimental temperature, i.e. $\theta = 60$ °C, and was found as $\left(\frac{\Delta L}{L}\right)_{\max} = -0.057$. If the material undergoes isotropic shrinkage due to UV curing, the chemical shrinkage strain is related to volumetric shrinkage as follows under the assumption of small strains [56, 57]:

$$\frac{\Delta L}{L}(q,\theta) = \frac{1}{3}\frac{\Delta V}{V_0}(q,\theta) \tag{26}$$

This equation yields the maximum volumetric shrinkage value to $\left(\frac{\Delta V}{V}\right)_{\max} = 17.1\%$. If it is considered that the maximum shrinkage value obtained by fitting the equation in the previous article [37] is around $\left(\frac{\Delta V}{V}\right)_{\max} = 16\%$, it can be concluded that approximately similar results can be obtained for maximum curing carried out under different conditions with different test methods. In the previous study, although the sample curing and tests were performed at room temperature, higher degrees of cure were attained as a consequence of exposure to more and longer UV light energy. Therefore, it can be said that it is possible to compare these two results and that these results are similar.

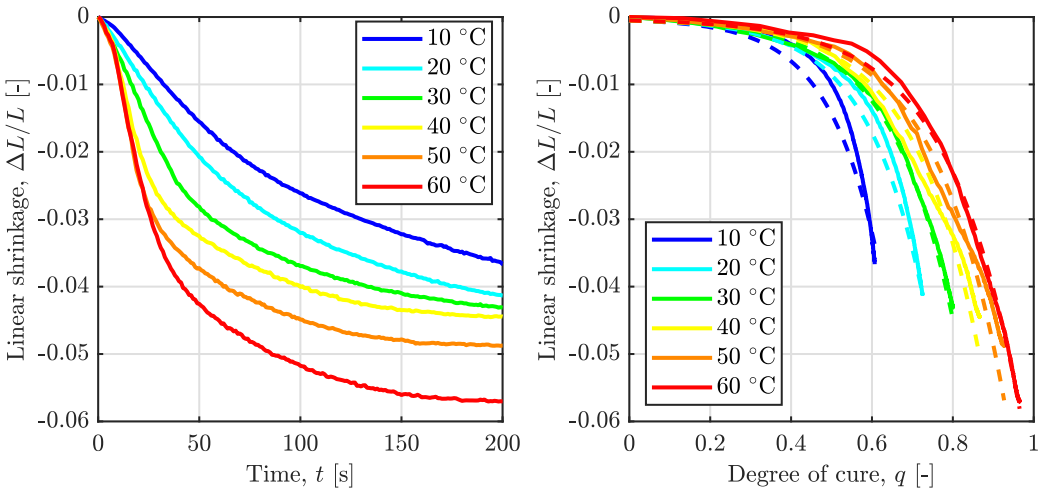

Figure 16: Experimentally measured chemical shrinkage at different isothermal conditions ($\theta = 10, 20, 30, 40, 50, 60$ °C) and constant frequency $f = 1$ Hz using UV rheometer tests. Left: Evolution with the curing time t. Right: Evolution with the degree of cure q and prediction results obtained by Equations 24 and 25.

Table 7: Parameters of the linear shrinkage function defined by Equations 24 and 25.

Parameter	α	β_1	β_2
Value [-]	2.5×10^{-4}	7.8×10^{-2}	2×10^{-1}

6. Conclusion and perspectives

This work offers a new perspective on the development of a comprehensive thermomechanical model required for the prediction of material properties during and after the photopolymerization reaction by experimental methods. We focus on the effect of the degree of cure, temperature and frequency on the viscoelastic properties and chemical shrinkage of the photopolymer materials. The change of viscoelastic properties and chemical shrinkage due to the UV light induced-crosslinking progress, the conventional rheometer consisting of parallel plates was upgraded with an UV light source and accessories that allow to control the temperature. Thus, time sweeping tests were performed in the controlled isothermal environment and at constant frequencies during the UV irradiation. Unfortunately, improvements are still needed to enhance the quality of the measurements and better integrate them

into the material modelling to consider the temperature effect during the UV curing. The measurements, however, revealed the expected qualitative improvement of viscoelastic properties during constant UV irradiation. During these tests, chemical shrinkage due to isothermal condition and curing has been calculated and a model equation based on these two parameters has been proposed. The time-cure superposition was applied to the UV rheometer tests carried out at 20 °C to perform material modelling during curing. DMA measurements of the samples that had been cured beyond the gelation point were performed in order to assess and simulate the viscoelastic material properties during the whole curing process. Then, the results from the UV rheometer and DMA were combined and the material modelling was completed during the whole curing.

The established modelling framework offers a useful insight to design the photopolymerization-based 3D printed structures, hence improving production efficiency and final material properties to produce desired parts. As the next stage of this study, the viscoelastic material modelling can be extended by a more generalized time-cure superposition that takes into account the effect of the maximum attainable degree of cure at different temperatures and light intensities during curing, and the effect of glass transition temperature after curing. The future work will involve incorporating those materials modelling into a finite element (FE) simulation methodology, that couples the effects of all pertinent mechanisms, to optimize the 3D printing process.

Acknowledgement

The financial support of the project "Constitutive modelling of UV-curing printed polymer composites" by the Agence nationale de la recherche (ANR) and the German Research Foundation (DFG) under the grant numbers ANR-18-CE92-0002-01 and LI 696/20-1 is gratefully acknowledged.

Conflicts of Interest

The authors declare no conflict of interest.

Appendix A. Modelling of the crosslinking reaction

Tables A.8 and A.9 list the maximum attainable degrees of cure $q_{\max}$ for all measurements and the identified model parameters, respectively.

Table A.8: Temperature- and UV light intensity-dependent maximum attainable degree of cure $q_{\max}(\mathcal{I}, \theta)$ for all measurements [37].

Temperature (°C)	$\mathcal{I} = \mathbf{5\ mW/cm^2}$	$\mathcal{I} = \mathbf{10\ mW/cm^2}$
10	0.635	0.742
20	0.757	0.813
30	0.829	0.872
40	0.893	0.918
50	0.951	0.961
60	0.988	0.996

Table A.9: Identified parameters of the model equation for the degree of cure q [37].

Parameter	**Value**	**Unit**	**Description**
A_1	0.135	1/s	Pre-exponential factor of the first Arrhenius coefficient
A_2	0.237	1/s	Pre-exponential factor of the second Arrhenius coefficient
E_1	2003.184	J/mol	Activation energy of the first Arrhenius coefficient
E_2	2005.08	J/mol	Activation energy of the second Arrhenius coefficient
m	1.848	-	Exponent of the first reaction
n	2.2	-	Exponent of the second reaction
b	0.627	-	Scaling factor of the influence of the light intensity
h_{tot}	-404.43	J/g	Total specific heat of reaction

Appendix B. UV rheometry measurements

In Figure B.17, the direct measurement results of the rheometer tests are given, including the conditioning period without any UV light being applied for the first 60 seconds.

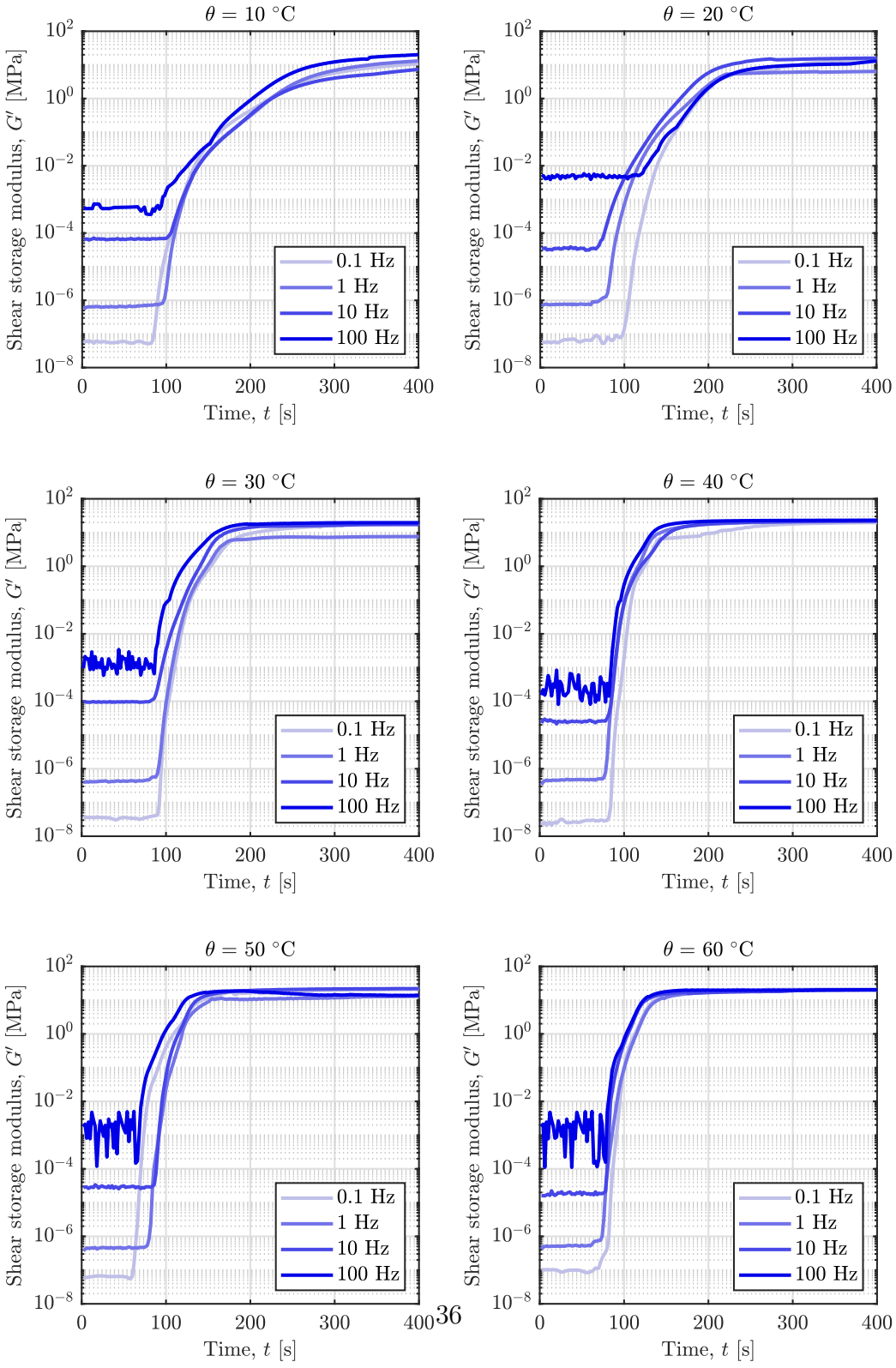

Figure B.17: Evolution of the shear storage modulus G' as a consequence of progressing UV curing in the photopolymer layer at different frequencies and isothermal conditions.

Appendix C. Evolution of the viscoelastic properties after the UV curing reaction

Appendix C.1. DMA measurements: Amplitude sweep tests - damping factor

The damping factors measured by DMA for samples at different curing states are presented in Figure C.18. It was observed that the damping factor decreases as the degree of cure increases.

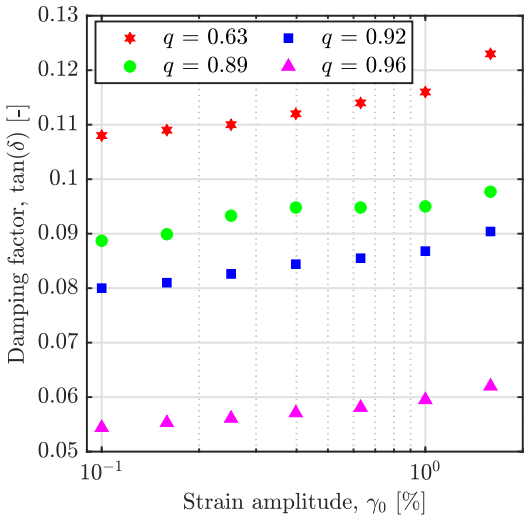

Figure C.18: Damping factors as a function of strain amplitude at $f = 1$ Hz and $\theta = 20$ °C for the samples with different degrees of cure $q = 0.63, 0.89, 0.92, 0.96$.

Appendix C.2. DMA measurements: Frequency sweep tests - shear loss moduli

The loss moduli results measured by DMA for 4 samples with different degrees of cure are given in Figure C.19. The frequency sweep test at different isothermal conditions revealed that the loss moduli at low temperatures were almost independent of the degree of cure. For all samples, the loss moduli decrease with increasing temperature, and this decrease is greater with decreasing degree of cure.

Using these measurements with storage moduli results, the time-temperature superposition was applied and Maxwell elements were identified.

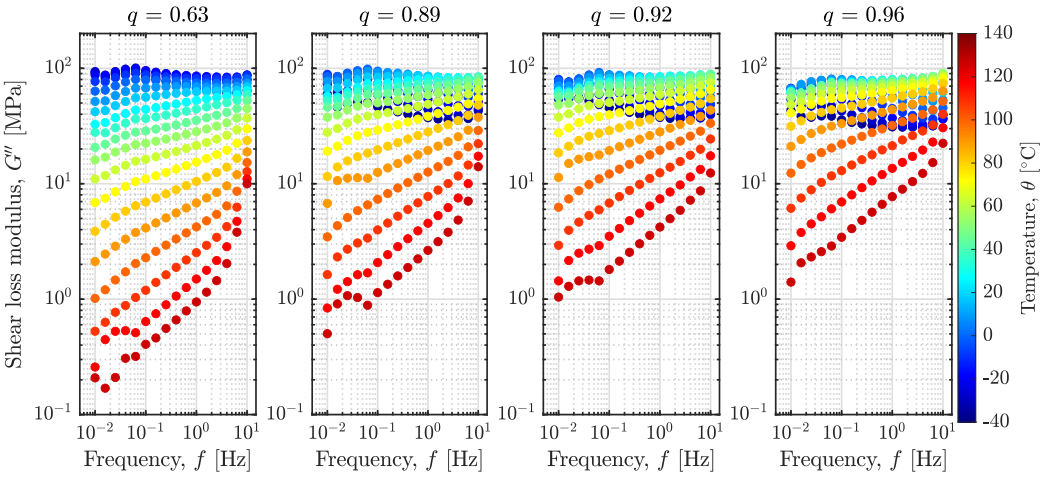

Figure C.19: Isothermal frequency sweep curves of the shear storage modulus G'' obtained from the DMA tests of the samples with different degrees of cure $q = 0.63, 0.89, 0.92, 0.96$.

Appendix C.3. Time-temperature superposition

Figure C.20 shows a comparison of the master curves obtained by shifting the isothermal curves of samples at different curing states (see Figure 11) using the TTSP and using the shift factors computed by fitting the WLF equation given in Equation 16.

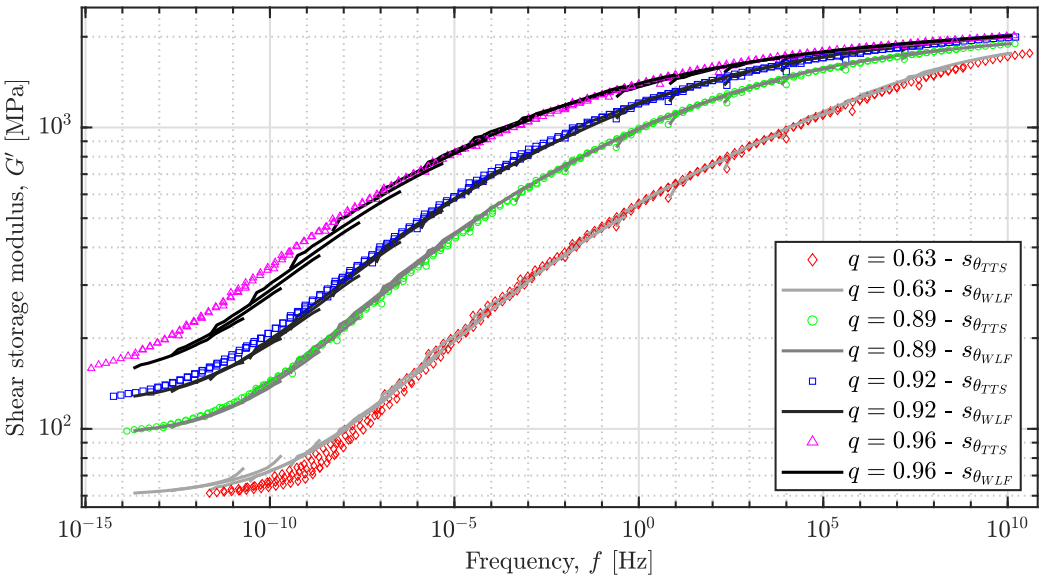

Figure C.20: Comparison of the master curves obtained by shifting the isothermal curves given for different samples in Figure 11 by applying TTSP and using the shift factors calculated by fitting the WLF equation given by Equation 16.

Appendix C.4. Identification of relaxation times and stiffnesses at the reference point

Appendix C.4.1. Schematic representation of a generalized Maxwell model

Figure C.21 shows a schematic representation of a generalized Maxwell model with n elements as a part of the rheological network.

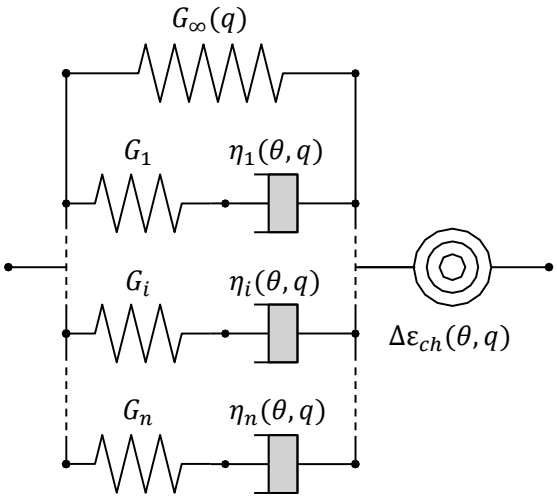

Figure C.21: Rheological network of the proposed model considering the mechanical and chemical deformations of the photopolymers. $\Delta\varepsilon_{ch}(\theta,q)$ represents the degree of cure- and temperature-dependent material parameter for the chemical shrinkage. The left part in which n Maxwell elements are connected in parallel represents degree of cure- and temperature-dependent the generalized Maxwell model considering viscoelastic deformations. A spring assumed independent of degree of cure and temperature spring G_i and a degree of cure- and temperature-dependent dashpot $\eta_i(\theta,q)$ are connected in series for each Maxwell element. An additional spring is connected in parallel to represent the equilibrium modulus $G_\infty(q)$.

Appendix C.4.2. Selection of number of Maxwell elements

Before the identification procedure on the master curve selected as a reference, the relaxation times must be distributed by selecting a set of n relaxation times evenly spaced on a logarithmic scale, i.e. $\lambda_{i+1} = a \times \lambda_i$. The logarithmic step between each relaxation time, denoted by a, can be calculated from the maximum and minimum relaxation times as follows [58]:

$$a = \left(\frac{\lambda_{\max}}{\lambda_{\min}}\right)^{\frac{1}{n-1}} \tag{C.1}$$

if the relaxation times are distributed far apart, this model tends to yield a loss modulus G'' (or damping factor $\tan(\delta)$) that exhibits oscillations. By choosing an appropriate a value that gives the best graphic result with the least possible oscillation and minimal error avoiding overestimation, the relaxation times are distributed in a range corresponding to the frequencies of the master curve for the identification of G_i consistent with the measure-

ments.

The reference point (i.e. the master curve of the DMA test) for the identification of Maxwell elements was chosen as $q = 0.96$ and $\theta_{ref} = 20$ °C. The following objective function was proposed to determine relaxation times λ_i, stiffnesses G_i and equilibrium modulus G_∞ in the weighted sum method:

$$r = \min_{G_i, G_\infty} \sum_{i=1}^{R} \left(w_1 \sqrt{\frac{\left|G'_{exp,i} - G'_{sim,i}\right|^2}{\left|G'_{exp,i}\right|^2}} + w_2 \sqrt{\frac{\left|G''_{exp,i} - G''_{sim,i}\right|^2}{\left|G''_{exp,i}\right|^2}} \right) \tag{C.2}$$

where R is the number of regression points, $G_{exp,i}$ are the experimental shear moduli at regression point i, $G_{sim,i}$ are the simulated shear moduli at regression point i, w_1 and w_2 are weight parameters selected as $w_1 = w_2 = 1$ for all identification procedure. Given that the storage modulus in the measurements is about 10 times greater than the loss modulus, this objective function has the advantage that high and low values have same weight on minimization. Maxwell elements were determined using the nonlinear least square fit of Matlab's [55] built-in routine, `lsqnonlin`, with the Levenberg-Marquardt algorithm, which minimizes the residual r on the proposed objective function given in Equation C.2 by constraining the algorithm as $G_i, G_\infty \geq 0$.

To find the optimum number of Maxwell elements, the residual values corresponding to the various a values were examined as in Figure C.22. It has been noticed that using more than 30 Maxwell elements results in overestimation, the residual value r of the objective function to reach plateau (see Figure C.22), and does not reduce the oscillations in the graphical display. As a result, it was decided to use 30 Maxwell elements in order to minimize the oscillating nature of the shear loss modulus. Figure C.23 compares the measured and simulated shear storage and loss moduli as a consequence of the identification of the viscoelastic spectrum at the reference point. The identified Maxwell parameters are listed in Table C.10. As can be seen, parameters that have been identified provides fitting globally closer to the experimental findings.

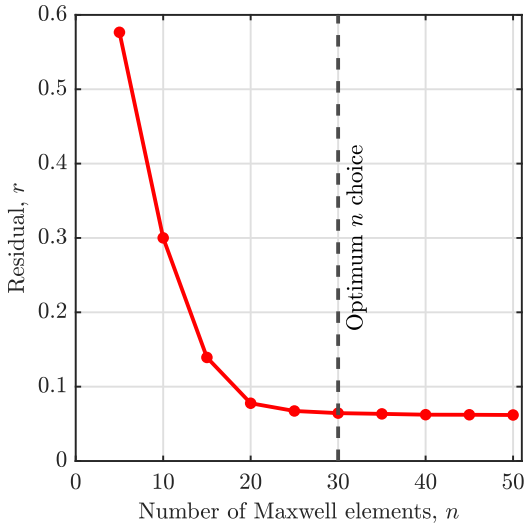

Figure C.22: Change of the residual value of the objective function given in Equation C.2 corresponding to different number of Maxwell elements n, to determine the optimum number of elements that should be selected for the best representation of the long-term viscoelastic material behaviour for $\theta_{ref} = 20$ °C and $q_{ref} = 0.96$ given in Figure C.20.

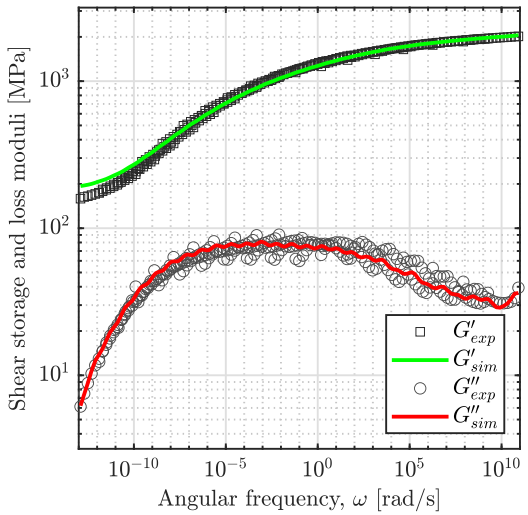

Figure C.23: Simulation of the generalized Maxwell model at the reference point $\theta_{ref} = 20$°C and $q_{ref} = 0.96$.

Appendix C.4.3. Identified Maxwell parameters

The identified Maxwell parameters are listed in Table C.10.

Table C.10: Identified Maxwell parameters at the reference point $\theta_{ref} = 20°\text{C}$ and $q_{ref} = 0.96$: stiffnesses G_i and relaxation times λ_i^{ref}.

i	**Stiffness, G_i [MPa]**	**Relaxation time, λ_i^{ref} [s]**
1	62.619	1.21E-11
2	26.247	8.05E-11
3	41.013	5.33E-10
4	41.009	3.53E-09
5	38.959	2.34E-08
6	50.239	1.55E-07
7	44.231	1.03E-06
8	63.694	6.82E-06
9	56.284	4.52E-05
10	75.671	3.00E-04
11	74.287	1.99E-03
12	81.196	1.32E-02
13	86.886	8.72E-02
14	90.128	5.78E-01
15	88.696	3.83E+00
16	93.597	2.54E+01
17	90.477	1.68E+02
18	98.308	1.11E+03
19	91.596	7.39E+03
20	92.698	4.90E+04
21	91.951	3.25E+05
22	83.760	2.15E+06
23	78.426	1.43E+07
24	70.628	9.45E+07
25	58.337	6.26E+08
26	46.875	4.15E+09
27	33.911	2.75E+10
28	22.485	1.82E+11
29	14.780	1.21E+12
30	6.754	8.01E+12

Appendix C.5. Time-cure superposition

Appendix C.5.1. Residual analysis

The residual value r increases with decreasing degree of cure, as listed in Table C.11, compared to the reference result at $q = 0.96$.

Table C.11: Residual values r between experimental master curves and simulation results depending on the degree of cure q calculated by Equation C.2.

Degree of cure, q [-]	**Residual values, r [-]**
0.63	0.2599
0.89	0.1547
0.92	0.1492
0.96	0.0644

Appendix C.5.2. Degree of cure-dependent equilibrium stiffness

Figure C.24 presents the comparison of experimental and simulated results for the equilibrium modulus $G_\infty(q)$. It should be noted that this model is valid for degrees of cure above the gelation point tested in DMA.

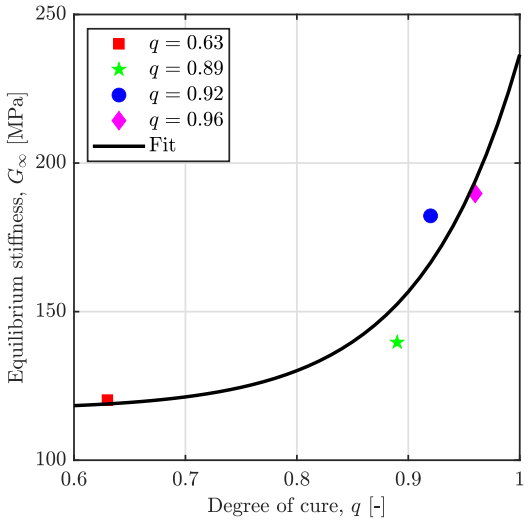

Figure C.24: Degree of cure-dependent equilibrium stiffness $G_\infty(q)$ and fitted curve using Equation 21.

Appendix D. Time-cure superposition for the entire curing process

To combine the shift findings from UV rheometer measurements with those from DMA measurements, the shift factors up to $q = 0.63$ acquired as a consequence of the UV rheometer tests at $\theta = 20$ °C given in Figure 7 were vertically and equally shifted downwards by $10^{-8.5}$ to build a continuous

curve with the shift factors obtained from the DMA measurements as shown in Figure D.25.

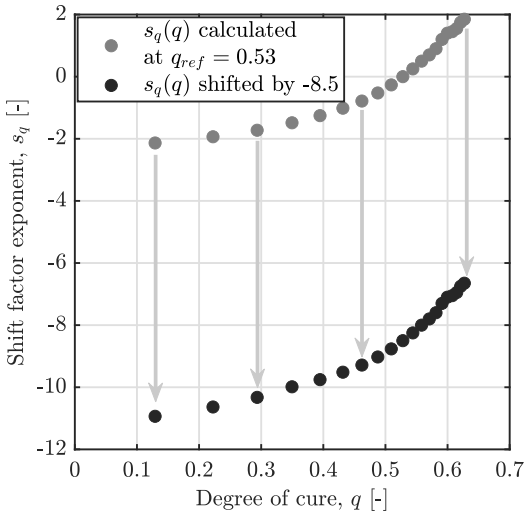

Figure D.25: Equally shifting the shift factor exponents to the base 10 $s_q(q)$ by -8.5 to build continuous $q - s_q$ curve for the time-cure superposition in the entire curing process at $\theta = 20$ °C.

Appendix E. Polymerization shrinkage - $\beta(\theta)$ function

The natural logarithm of the $\beta(\theta)$ function and temperature values were taken to establish a relationship between function $\beta(\theta)$ and temperature θ, as shown in Figure E.26. To better address the experimental results, the following equation is suggested as a curve-fitting method for the linear relationship found in the graph:

$$\beta(\theta) = \beta_1 \left(\frac{\theta}{\theta_0} \right)^{\beta_2} \tag{E.1}$$

where β_1 and β_2 are model parameters to be identified and $\theta_0 = 1$ °C is merely utilized to maintain unit consistency. Table 7 contains a list of the identified parameters for Equations 24 and E.1.

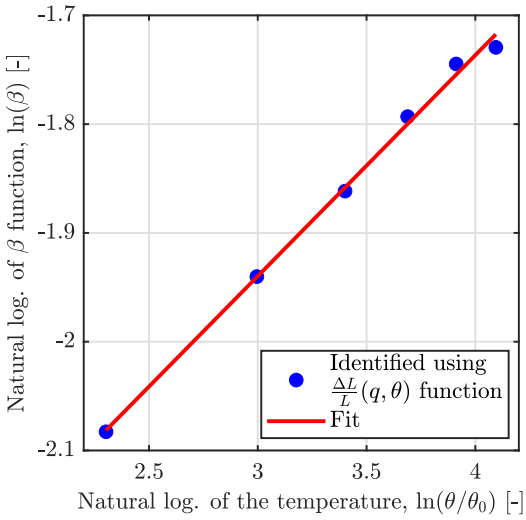

Figure E.26: Curve fitting by the identification of β_1 and β_2 parameters for $\beta(\theta)$ function: To begin with, the natural logarithm of the temperature-dependent results of the $\beta(\theta)$ function obtained from Equation 24 was taken (displayed by blue circles). Then, Equation 25 was fitted to represent the identified results.

References

[1] T. D. Ngo, A. Kashani, G. Imbalzano, K. T. Nguyen, D. Hui, Additive manufacturing (3D printing): A review of materials, methods, applications and challenges, Composites Part B: Engineering 143 (2018) 172–196.

[2] A. Al Rashid, W. Ahmed, M. Y. Khalid, M. Koc, Vat photopolymerization of polymers and polymer composites: Processes and applications, Additive Manufacturing 47 (2021) 102279.

[3] J. Plocher, A. Panesar, Review on design and structural optimisation in additive manufacturing: Towards next-generation lightweight structures, Materials & Design 183 (2019) 108164.

[4] A. Zhakeyev, L. Zhang, J. Xuan, Photoactive resin formulations and composites for optical 3D and 4D printing of functional materials and devices, in: 3D and 4D Printing of Polymer Nanocomposite Materials, Elsevier, 2020, pp. 387–425.

[5] N. A. Chartrain, C. B. Williams, A. R. Whittington, A review on fabricating tissue scaffolds using vat photopolymerization, Acta Biomaterialia 74 (2018) 90–111.

[6] Q. Mu, L. Wang, C. K. Dunn, X. Kuang, F. Duan, Z. Zhang, H. J. Qi, T. Wang, Digital light processing 3D printing of conductive complex structures, Additive Manufacturing 18 (2017) 74–83.

[7] Z. Ding, C. Yuan, X. Peng, T. Wang, H. J. Qi, M. L. Dunn, Direct 4D printing via active composite materials, Science Advances 3 (4) (2017) e1602890.

[8] L. R. Meza, S. Das, J. R. Greer, Strong, lightweight, and recoverable three-dimensional ceramic nanolattices, Science 345 (6202) (2014) 1322–1326.

[9] M. Layani, X. Wang, S. Magdassi, Novel materials for 3D printing by photopolymerization, Advanced Materials 30 (41) (2018) 1706344.

[10] J. R. Tumbleston, D. Shirvanyants, N. Ermoshkin, R. Janusziewicz, A. R. Johnson, D. Kelly, K. Chen, R. Pinschmidt, J. P. Rolland, A. Ermoshkin, et al., Continuous liquid interface production of 3D objects, Science 347 (6228) (2015) 1349–1352.

[11] Y. Shan, A. Krishnakumar, Z. Qin, H. Mao, Reducing lateral stair-stepping defects in liquid crystal display-based vat photopolymerization by defocusing the image pattern, Additive Manufacturing 52 (2022) 102653.

[12] J. G. Leprince, W. M. Palin, M. A. Hadis, J. Devaux, G. Leloup, Progress in dimethacrylate-based dental composite technology and curing efficiency, Dental Materials 29 (2) (2013) 139–156.

[13] J. J. Schwartz, Additive manufacturing: Frameworks for chemical understanding and advancement in vat photopolymerization, MRS Bulletin (2022) 1–14.

[14] C. Decker, The use of UV irradiation in polymerization, Polymer International 45 (2) (1998) 133–141.

[15] G. A. Appuhamillage, N. Chartrain, V. Meenakshisundaram, K. D. Feller, C. B. Williams, T. E. Long, 110th anniversary: Vat photopolymerization-based additive manufacturing: Current trends and future directions in materials design, Industrial & Engineering Chemistry Research 58 (33) (2019) 15109–15118.

[16] D. K. Patel, A. H. Sakhaei, M. Layani, B. Zhang, Q. Ge, S. Magdassi, Highly stretchable and UV curable elastomers for digital light processing based 3D printing, Advanced Materials 29 (15) (2017) 1606000.

[17] H. Cui, R. Hensleigh, D. Yao, D. Maurya, P. Kumar, M. G. Kang, S. Priya, X. R. Zheng, Three-dimensional printing of piezoelectric materials with designed anisotropy and directional response, Nature Materials 18 (3) (2019) 234–241.

[18] A. Maurel, A. C. Martinez, S. Grugeon, S. Panier, L. Dupont, P. Cortes, C. G. Sherrard, I. Small, S. T. Sreenivasan, E. MacDonald, Towards high resolution 3D printing of shape-conformable batteries via vat photopolymerization: review and perspective, IEEE Access (2021).

[19] M. Hossain, P. Steinmann, Degree of cure-dependent modelling for polymer curing processes at small-strain. part I: consistent reformulation, Computational Mechanics 53 (4) (2014) 777–787.

[20] D. F. Swinehart, The Beer-Lambert law, Journal of Chemical Education 39 (7) (1962) 333.

[21] C. I. Fiedler-Higgins, L. M. Cox, F. W. DelRio, J. P. Killgore, Monitoring fast, voxel-scale cure kinetics via sample-coupled-resonance photorheology, Small Methods 3 (2) (2019) 1800275.

[22] J. Wu, Z. Zhao, C. M. Hamel, X. Mu, X. Kuang, Z. Guo, H. J. Qi, Evolution of material properties during free radical photopolymerization, Journal of the Mechanics and Physics of Solids 112 (2018) 25–49.

[23] T. Rehbein, M. Johlitz, A. Lion, K. Sekmen, A. Constantinescu, Temperature- and degree of cure-dependent viscoelastic properties of photopolymer resins used in digital light processing, Progress in Additive Manufacturing 6 (4) (2021) 743–756.

[24] J. Zhou, Q.-y. Zhang, S.-j. Chen, H.-p. Zhang, A.-j. Ma, M.-l. Ma, Q. Liu, J.-j. Tan, Influence of thiol and ene functionalities on thiol–ene networks: Photopolymerization, physical, mechanical, and optical properties, Polymer Testing 32 (3) (2013) 608–616.

[25] F. Jiang, A. Wörz, M. Romeis, D. Drummer, Analysis of UV-assisted direct ink writing rheological properties and curing degree, Polymer Testing 105 (2022) 107428.

[26] M. Štaffová, F. Ondreáš, J. Svatík, M. Zbončák, J. Jančář, P. Lepcio, 3D printing and post-curing optimization of photopolymerized structures: Basic concepts and effective tools for improved thermomechanical properties, Polymer Testing 108 (2022) 107499.

[27] S. I. Kundalwal, A. Rathi, Improved mechanical and viscoelastic properties of CNT-composites fabricated using an innovative ultrasonic dual mixing technique, Journal of the Mechanical Behavior of Materials 29 (1) (2020) 77–85.

[28] D. Miedzińska, R. Gieleta, E. Małek, Experimental study of strength properties of SLA resins under low and high strain rates, Mechanics of Materials 141 (2020) 103245.

[29] B. J. Green, C. A. Guymon, Modification of mechanical properties and resolution of printed stereolithographic objects through raft agent incorporation, Additive Manufacturing 27 (2019) 20–31.

[30] E. A. Garcia, A. J. Qureshi, C. Ayranci, A study on material-process interaction and optimization for vat-photopolymerization processes, Rapid Prototyping Journal (2018).

[31] K. G. Mostafa, M. Arshad, A. Ullah, D. S. Nobes, A. J. Qureshi, Concurrent modelling and experimental investigation of material properties and geometries produced by projection microstereolithography, Polymers 12 (3) (2020) 506.

[32] H. Gojzewski, Z. Guo, W. Grzelachowska, M. Ridwan, M. Hempenius, D. Grijpma, G. Vancso, Layer-by-layer printing of photopolymers in 3D: How weak is the interface?, ACS applied materials & interfaces 12 (7) (2020) 8908–8914.

[33] M. Lebedevaite, J. Ostrauskaite, E. Skliutas, M. Malinauskas, Photocross-linked polymers based on plant-derived monomers for potential application in optical 3D printing, Journal of Applied Polymer Science 137 (20) (2020) 48708.

[34] D. A. Rau, J. P. Reynolds, J. S. Bryant, M. J. Bortner, C. B. Williams, A rheological approach for measuring cure depth of filled and unfilled photopolymers at additive manufacturing relevant length scales, Additive Manufacturing 60 (2022) 103207.

[35] Arkema N3xtDimension®- PR48 - Clear Prototyping Material: Technical Data Sheet, Available at https://cpspolymers.com/PR48%20TDS.pdf, accessed: 10/09/2022.

[36] EMBER ™- PR48 - Autodesk Standard Clear Prototyping Resin (PR48), Available at https://cdn2.hubspot.net/hubfs/1545937/Autodesk_Standard_Clear_PR48_Formulation.pdf?__hss, accessed: 10/09/2022.

[37] K. Sekmen, T. Rehbein, M. Johlitz, A. Lion, A. Constantinescu, Thermal analysis and shrinkage characterization of the photopolymers for DLP additive manufacturing processes, Continuum Mechanics and Thermodynamics (2022) 1–18.

[38] K. Sekmen, T. Rehbein, M. Johlitz, A. Lion, A. Constantinescu, Material modelling of the photopolymers for additive manufacturing processes, in: 2022 International Solid Freeform Fabrication Symposium, University of Texas at Austin, 2022, pp. 94–106.

[39] T. Rehbein, A. Lion, M. Johlitz, A. Constantinescu, Experimental investigation and modelling of the curing behaviour of photopolymers, Polymer Testing 83 (2020) 106356.

[40] J. D. Ferry, Viscoelastic properties of polymers, 3rd Edition, John Wiley & Sons, 1980.

[41] ISO 6721-2 - Plastics — Determination of dynamic mechanical properties — Part 2: Torsion-pendulum method, , International Organization for Standardization, Geneva, CH (2019).

[42] M. Di Francescantonio, T. R. Aguiar, C. A. G. Arrais, A. N. Cavalcanti, C. U. Davanzo, M. Giannini, Influence of viscosity and curing mode on degree of conversion of dual-cured resin cements, European Journal of Dentistry 7 (1) (2013) 81.

[43] H. H. Winter, F. Chambon, Analysis of linear viscoelasticity of a crosslinking polymer at the gel point, Journal of Rheology 30 (2) (1986) 367–382.

[44] ASTM D4473 - 08 - Standard Test Method for Plastics: Dynamic Mechanical Properties: Cure Behavior, Standard, ASTM International, West Conshohocken, PA, USA (2008).

[45] J. Lange, J.-A. E. Månson, A. Hult, Build-up of structure and viscoelastic properties in epoxy and acrylate resins cured below their ultimate glass transition temperature, Polymer 37 (26) (1996) 5859–5868.

[46] P. F. Jacobs, Rapid prototyping & manufacturing: fundamentals of stereolithography, Society of Manufacturing Engineers, 1992.

[47] D. Adolf, J. E. Martin, Time-cure superposition during crosslinking, Macromolecules 23 (15) (1990) 3700–3704.

[48] Y. Eom, L. Boogh, V. Michaud, P. Sunderland, J.-A. Månson, Time-cure-temperature superposition for the prediction of instantaneous viscoelastic properties during cure, Polymer Engineering & Science 40 (6) (2000) 1281–1292.

[49] ASTM D7175 - 08 - Standard Test Method for Determining the Rheological Properties of Asphalt Binder Using a Dynamic Shear Rheometer, Standard, ASTM International, West Conshohocken, PA, USA (2008).

[50] DIN 51810-2 - Testing of lubricants - Testing rheological properties of lubricating greases - Part 2: Determination of flow point using an oscillatory rheometer with a parallel-plate measuring system, Standard, Deutsches Institut für Normung e.V, Berlin, DE (2017).

[51] P. Butaud, V. Placet, J. Klesa, M. Ouisse, E. Foltete, X. Gabrion, Investigations on the frequency and temperature effects on mechanical properties of a shape memory polymer (Veriflex), Mechanics of Materials 87 (2015) 50–60.

[52] Z. Zhao, J. Wu, X. Mu, H. Chen, H. J. Qi, D. Fang, Desolvation induced origami of photocurable polymers by digit light processing, Macromolecular Rapid Communications 38 (13) (2017) 1600625.

[53] C. Gorsche, R. Harikrishna, S. Baudis, P. Knaack, B. Husar, J. Laeuger, H. Hoffmann, R. Liska, Real time-NIR/MIR-photorheology: a versatile tool for the in situ characterization of photopolymerization reactions, Analytical Chemistry 89 (9) (2017) 4958–4968.

[54] G. Sun, X. Wu, R. Liu, A comprehensive investigation of acrylates photopolymerization shrinkage stress from micro and macro perspectives by real time MIR-photo-rheology, Progress in Organic Coatings 155 (2021) 106229.

[55] Matlab online documentation, Available at `https://www.mathworks.com/help/`, accessed: 01/10/2022.

[56] T. Wu, Theoretical modeling and experimental characterization of stress and crack development in parts manufactured through large area maskless photopolymerization, Ph.D. thesis, Georgia Institute of Technology (2014).

[57] B. Fayolle, L. Audouin, G. George, J. Verdu, Macroscopic heterogeneity in stabilized polypropylene thermal oxidation, Polymer Degradation and Stability 77 (3) (2002) 515–522.

[58] A. Jouan, Influence du vieillissement en atmosphère confinée sur la prédiction de la durée de vie des joints adhésifs, Ph.D. thesis, Université Paris-Saclay (ComUE) (2018).